



# UNIVERSITY OF TWENTE.

**Faculty of Engineering Technology  
Mechanical Engineering  
Dynamics Based Maintenance**

## **Experimental and structural load assessment in wind turbine drive trains**

**Remco J. van Dasselaar**  
**Master Thesis**  
**February 2019**  
**Enschede**

---

**Exam committee:**

Prof. dr. ir. T. Tinga  
Ir. D.P. Rommel  
Dr. ir. J.P. Schilder

Department of Mechanics of Solids, Surfaces & Systems  
Faculty of Engineering Technology  
University of Twente  
P.O. Box 217  
7500 AE Enschede  
The Netherlands

s1489909  
r.j.vandasselaar@alumnus.utwente.nl

Documentnumber: ET.191TM-5849

---



# Summary

Wind turbine components fail before their statistical based predicted lifetime. The statistic prediction is difficult because of varying parameters in side conditions, components and loads. Early component failures are mostly unexpected and thus costly maintenance.

Improvement in lifetime prediction can be done by using the actual internal loads in a wind turbine. Lifetime prediction based on a failure model with internal loads as input can take into account the variations and adjust the lifetime prediction based on measurements. The internal loads can be determined with a structural model of the wind turbine using accelerometers as input. Therefore this research focuses on the feasibility of a structural model for the load prediction of wind turbines.

Three different approaches as structural model are considered: based on analytic dynamics, using Finite Element Method (FEM) program Spacar and a manually defined FEM model. All three approaches are applied to a test bench; the manually defined FEM method appears to be the most suitable. The structural model is validated by comparing frequencies of the model and an hammer impact test (HIT) on the test bench. A force amplitude comparison between the prediction using acceleration measurements and the theoretical force due to the centrifugal acceleration showed predictions with about 50% error. Possible causes are discussed and recommendations are given to improve the accuracy.

Also an outlook is given with a bearing force prediction based on acceleration measurements.



# Preface and acknowledgements

Dear reader, this report describes the results of my master thesis done at the Dynamics Based Maintenance chair of mechanical engineering at the University of Twente. This exciting topic about wind turbine vibrations in combination with dynamics fascinated me already in the first years of my study. I enjoyed working with the vibrating test bench in the acoustics laboratory, which was not only fun but also a challenge to capture the dynamics in a structural model using different approaches. As usual in science the final result is most of the times different than expected; I hope you (as well) still enjoy reading this report. It feels weird painting as an artist using Latex and Inkscape magic to get this final result on paper.

I would like to praise the One for whom are all things, and by whom are all things [1].

I would like to thank some people for advise and help during my thesis. First, Damian, thank you for the possibility to do this assignment. Thank you for your advise you gave during our meetings, not only about the topic, but also regarding future work at a company. Also thank you for your feedback on the report to professionalize the end result. Tiedo, thank you for your feedback on my presentations and report. Dustin, thank you for working together to build the test bench. André, Dario, Jurnan, Richard and Ronald, thank you all for advise regarding Dynamics, the Finite Element Method and Spacar. I would like to thank my fellow students Adriaan, Bjorn, Casper, Coen, Gert-Jan, Hans and Sven for drinking coffee together but at the same time brainstorm about struggles I encountered. Adriaan, Feite and Nikita, thank you all for feedback on my report, it is peculiar to read your own words back and discover the chaos of them. Axel, thank you for your practical support and advice regarding the test bench.

Marlies, thanks for believing in me.

Mum and dad, thank you both for your love; believing in me and stimulating me in the world of technique and mechanics from early childhood.

Robert, thank you for your hospitality at wind turbine manufacturer and developer Lagerwey in Barneveld, which gave me a better understanding and engineering feeling about the design and construction of direct drive wind turbines. This was a nice connection between my theoretical work and the application done in the field.

*Remco van Dasselaar*  
*Enschede, February 2019*



# List of Symbols

## Roman

<b>A</b>	dynamic stiffness matrix	[multiple]
<i>A</i>	cross sectional area	[m <sup>2</sup> ]
<b>a</b>	acceleration measurements vector	[m s <sup>-2</sup> ]
<i>a</i>	node numbering	[-]
$\hat{a}$	maximum excitation	[dB]
<b>B</b>	analytic beam modeshape coefficients vector	[-]
<i>b</i>	node numbering	[-]
<b>C</b>	damping matrix	[multiple]
<i>C</i>	basic dynamic load rating from bearing geometry	[N]
<b>D</b>	modeshape trigonometric functions matrix	[-]
<i>d</i>	diameter	[m]
<i>E</i>	Young's modulus	[Pa]
<i>F</i>	force	[N]
<i>f</i>	distributed load	[N m <sup>-1</sup> ]
<i>G</i>	shear modulus	[Pa]
<i>g</i>	gravity constant	[m s <sup>-2</sup> ]
<i>I</i>	second moment of inertia	[m <sup>4</sup> ]
<i>h</i>	beam height	[m]
<i>J</i>	mass inertia	[kg m <sup>2</sup> ]
<b>K</b>	stiffness matrix	[multiple]
$\hat{\mathbf{K}}$	reduced stiffness matrix	[multiple]
<i>k</i>	stiffness	[multiple]
<i>L</i>	total beam length	[m]
<i>L</i>	basic rating life reliability	[millions of revolutions]
<i>l</i>	beam section element length	[m]
<b>M</b>	mass matrix	[multiple]
$\hat{\mathbf{M}}$	reduced mass matrix	[multiple]
<i>M</i>	bending moment	[N m]
<i>m</i>	mass beam element section	[kg]
<i>N</i>	gear ratio	[-]
<i>n</i>	Eigenmode number	[-]
<i>n</i>	amount of gear teeth	[-]
<i>P</i>	equivalent dynamic bearing load	[N]
<i>p</i>	exponent for the bearing life equation	[-]
<b>Q</b>	load vector	[N]
<b>q</b>	beam coordinates vector	[multiple]
<b>R</b>	load vector	[multiple]
<i>r</i>	radius	[m]
<i>r'</i>	non-dimensional radius of gyration	[-]
<i>T</i>	transient modeshape	[-]
<i>T</i>	torque	[N m]
<i>t</i>	time	[s]
<i>W</i>	spatial modeshape	[-]
<i>w</i>	radial beam deflection	[m]
<i>w</i>	gear width	[m]
<b>Y</b>	acceleration amplitude	[m s <sup>-2</sup> ]
<i>Z</i>	spatial amplitude	[-]

## Greek

$\alpha$	Rayleigh damping coefficient	[rad]
$\alpha$	scaling factor modeshapes	[m]
$\beta$	wave number	[m <sup>-1/4</sup> ]
$\beta$	Rayleigh damping coefficient	[rad <sup>-1</sup> ]
$\gamma$	acceleration equation	[multiple]
$\delta$	distance	[m]
$\delta_{ij}$	Kronecker delta	[-]
$\epsilon$	coordinate displacements Spacar	[-]
$\zeta$	damping ratio	[-]
$\eta$	natural coordinate	[multiple]
$\eta$	gearbox rotation around $x$ -axis	[rad]
$\theta$	rotation about $y$ -axis	[rad]
$\lambda$	Lagrange multiplier	[-]
$\mu$	rotary frequency factor	[-]
$\rho$	density	[kg m <sup>-3</sup> ]
$\Phi$	constraints matrix	[multiple]
$\phi$	rotation about $y$ -axis	[rad]
$\psi$	rotation about $x$ -axis	[rad]
$\Omega$	rotor rotational speed	[rad s <sup>-1</sup> ]
$\omega$	beam resonance frequency	[rad s <sup>-1</sup> ]

## Abbreviations

ac	accelerometer
B	bearing
CAD	computer aided design
CMS	condition based maintenance
DoF	degree of freedom
FEM	finite element method
GEN	generator
GB	gearbox
HIT	hammer impact test
HSS	high speed shaft
INT	intermediate shaft
LSS	low speed shaft
SCADA	supervisory control and data acquisition
SHM	structural health monitoring



# Contents

<b>1</b>	<b>Introduction</b>	<b>1</b>
1.1	Background . . . . .	1
1.2	Current lifetime prediction . . . . .	1
1.2.1	Lifetime prediction during design . . . . .	1
1.2.2	Lifetime prediction during operation . . . . .	2
1.3	Problem statement . . . . .	3
1.4	Research questions . . . . .	3
1.5	Approach . . . . .	3
1.6	Drive train configuration . . . . .	5
1.7	Test bench . . . . .	6
1.7.1	Description . . . . .	6
1.7.2	Excitation force . . . . .	6
1.7.3	Rotary inertia effect for rotating shafts . . . . .	7
1.7.4	Rotary effects at the rotor . . . . .	8
<b>2</b>	<b>Methodology</b>	<b>11</b>
2.1	Analytic structural model . . . . .	11
2.1.1	Modeshapes . . . . .	11
2.1.2	Modeshape scaling . . . . .	12
2.1.3	Harmonic forced vibration . . . . .	13
2.2	FEM structural model . . . . .	14
2.2.1	Spacar . . . . .	14
2.2.2	Manual program . . . . .	14
<b>3</b>	<b>Application</b>	<b>19</b>
3.1	Analytic . . . . .	19
3.2	FEM - Spacar . . . . .	22
3.3	FEM - Defined manually . . . . .	22
3.3.1	Elements . . . . .	22
3.3.2	Boundary conditions . . . . .	23
3.3.3	Link LSS to Base . . . . .	24
3.3.4	Link between GB, LSS and HSS . . . . .	25
<b>4</b>	<b>Data processing</b>	<b>29</b>
4.1	Acceleration measurements filtering . . . . .	29
4.2	From acceleration measurements to loads . . . . .	29
4.2.1	Structural model inputs . . . . .	30
4.2.2	Manipulation of dynamic stiffness matrix $\mathbf{A}$ . . . . .	30
4.2.3	Structural model output . . . . .	31
4.3	From theoretical rotor force to accelerations . . . . .	31
4.3.1	Structural model inputs . . . . .	31
4.3.2	Manipulation of dynamic stiffness matrix $\mathbf{A}$ . . . . .	32
4.3.3	Structural model output . . . . .	32
<b>5</b>	<b>Validation results and discussion</b>	<b>33</b>
5.1	Sensor validation . . . . .	33
5.2	Modes validation . . . . .	34
5.2.1	Hammer Impact Test (HIT) . . . . .	34
5.2.2	Rotor speed sweep . . . . .	34
5.2.3	Model modeshapes . . . . .	35
5.2.4	Comparison between HIT and FEM modeshapes . . . . .	36

5.2.5	Model consistency . . . . .	37
5.2.6	Damping . . . . .	37
5.3	Predict accelerations using assumed rotor force . . . . .	38
5.3.1	Acceleration comparison for one specific rotational speed . . . . .	38
5.3.2	Acceleration comparison for a range of rotational speeds . . . . .	38
5.4	Load prediction using accelerations . . . . .	39
5.4.1	Rotor load prediction at one constant rotational speed . . . . .	39
5.4.2	Rotor force prediction for a range of rotational speeds . . . . .	40
5.5	Discussion . . . . .	40
<b>6</b>	<b>Outlook</b>	<b>41</b>
6.1	Prediction at one constant rotational speed . . . . .	41
6.2	Bearing load prediction for a range of rotational speeds . . . . .	42
<b>7</b>	<b>Conclusion</b>	<b>43</b>
<b>8</b>	<b>Recommendations</b>	<b>45</b>
<b>A</b>	<b>Test bench description</b>	<b>51</b>
A.1	Design . . . . .	51
A.2	Dimensions and properties test bench . . . . .	52
<b>B</b>	<b>Matlab program description</b>	<b>55</b>
B.1	Parameters definition . . . . .	55
B.2	Analytic model . . . . .	55
B.3	Spacar . . . . .	55
B.4	FEM . . . . .	55
B.4.1	Model . . . . .	55
B.4.2	Data preprocessing . . . . .	56
B.4.3	Loads to accelerations . . . . .	56
B.4.4	Acceleration to loads . . . . .	56

# 1 Introduction

## 1.1 Background

Nowadays, conversion from wind to electrical energy is done on a large scale using wind turbines, both on- and offshore. To become more and more competitive with fossil fuel energy, a reduction in costs is needed, which can, among others, be reached with a more economic operation and maintenance strategy [2, 3]. For offshore a lot of planning in the maintenance strategy is involved, since it is much more difficult to get equipment, materials and employees at the right spot at sea compared to onshore wind turbines. Unexpected failures on offshore wind turbines are therefore much more costly. A failure can be defined as the state of a system when it can not longer fulfil its intended or designed function. In general, a failure is a result of the loads on a system exceeding the system capacity [4], caused by:

1. The capacity can be too low by a weak design, for example by using too small geometry dimensions. Designs are over-sized and have too much capacity to be on the 'safe side'. In general, the capacity is determined during the design phase and can not (easily be) changed afterwards.
2. The loads can be too high by underestimation. To be on the 'safe side', loads are overestimated resulting in replacing components before the end of their lifetime, leaving a part of it unused.

Both determining the capacity and loads are important for wind turbines, since most components have to last their entire lifespan of about twenty years. Ideally, only small maintenance is performed during these years, for example lubrication. However, in practise many wind turbine components fail before their required lifetime [5]. Apparently, the estimations of the capacity or loads are inadequate. Loads exceeding the capacity result in too high internal loads causing (internal) component failure. The relation between usage (loads) and lifetime is schematically shown in figure 1.1. Several methods to describe this relation (shown as system in the blue box) are discussed in the next section.

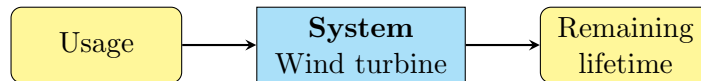


Figure 1.1: Lifetime is determined by the usage of the system, adapted from [4].

## 1.2 Current lifetime prediction

The current lifetime prediction is done during the design and during the operation of a wind turbine. This section describes how this prediction is done at both wind turbine life stages.

### 1.2.1 Lifetime prediction during design

Most research to wind turbine design and maintenance in literature focuses on the statistic description of wind speed and turbulence, since there is no exact solution to determine it. The predictions are used as input for multi-body dynamics in combination with the Finite Element Method (FEM) for multiple flexible components, (for example programs like Simpack [6] or Adams). These are used as structural model to estimate the local loads and determine the needed capacity during the design phase, using a given failure model by standards or manufacturers. This method is visualized in figure 1.2, with figure 1.1 shown in a grey box. However, the wind load is predicted (extrapolated) with a certain error, shown by comparing statistical probability functions with measurements from the field [7]. Differences between these can be due to variation in site conditions [8] and manufacturing quality [9]. These differences can lead to a negative balance of capacity and loads, with the consequence of failures.

Also component failure is tried to predict using statistics. It is mainly applied on the bending of rotor blades and the tower, without using a physical model of the structural dynamics [10].

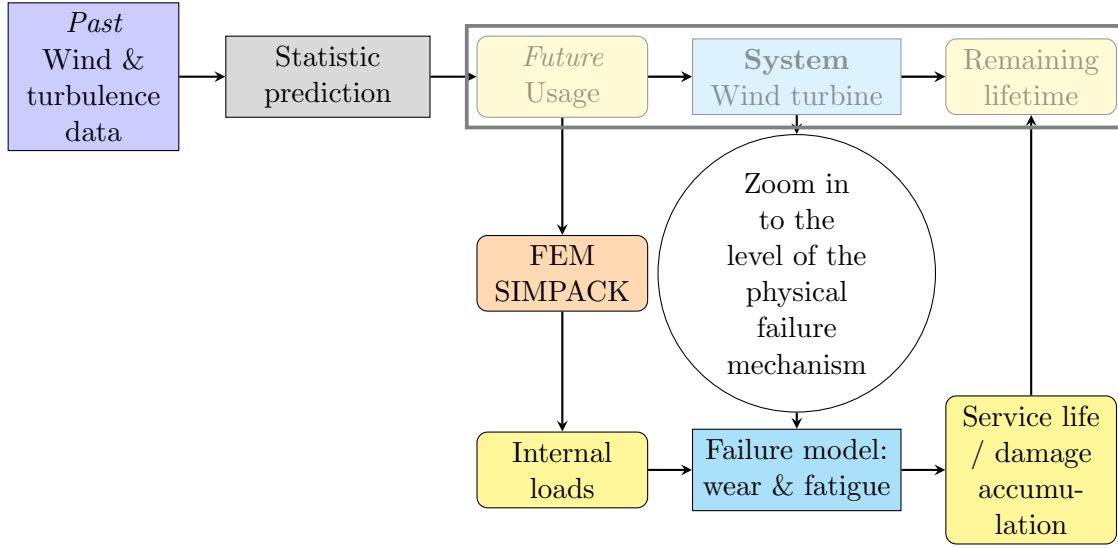


Figure 1.2: Statistics to predict wind speed & turbulence in combination with FEM to design the wind turbine and achieve a required lifetime, adapted from [4].

### 1.2.2 Lifetime prediction during operation

The statistical approach during design is basically a 'feed forward control', since data is measured in advance and used to 'control' the lifetime of a system. To make it more like 'feed back control', real-time measurements during operation can be used to control the lifetime. This is called a Condition Monitoring System (CMS). The basic system is a so called Supervisory Control and Data Acquisition (SCADA) system, which is present on almost every wind turbine. This system samples characteristic quantities like the power generation, wind speed, nacelle temperature, gearbox oil and bearing temperatures, generator winding temperatures and phase currents at fixed intervals. It is able to alarm operators, but cannot give inside information.

More detailed systems consider Structural Health Monitoring, aiming on determining the integrity of the structure [11]. Active displacement measurements is done at the blades measuring strain, but the relation between strains and stresses is not given [12]. In another research by Hameed et al. [13], CMS is applied to the drive train of wind turbines using accelerometers and vibration analyses. The data is used in probability models, but it is hard to validate these due to slow degradation and failure mechanisms. The data process is shown in figure 1.3, which is an extension to figure 1.1, shown as box. Field measurements are processed using classification to predict the remaining lifetime. For example, high vibrations mean a component failure probably. The classification is not about a periodic movement, such as structural vibrations or fatigue cycles, but rather an offset of the normal excitation caused by an impurity or irregularity in a component. Besides using a statistical model, also structural models are used to describe

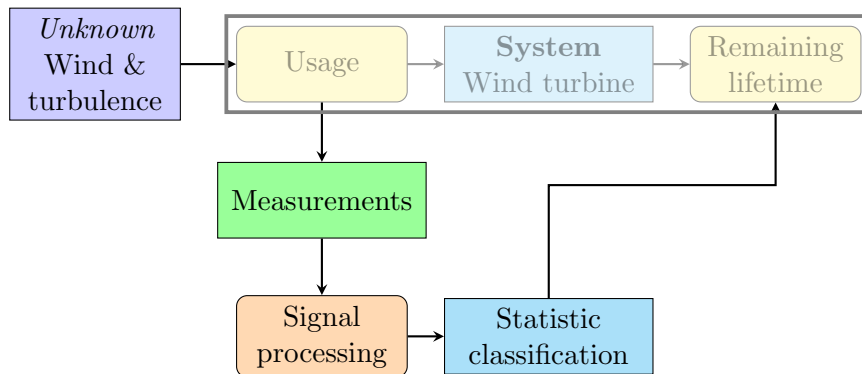


Figure 1.3: Condition Monitoring System applied to a wind turbine.

the relation between external and internal loads. Wasilczuk et al. [14] mention determining internal loads, but his approach and results are not available. Research to drive train modelling

and failures already takes place, considering shaft bending, bearing clearance and tolerances [5]. CMS is applied using measurements of different characteristic quantities, for example vibrations, acoustics, electrical output and oil quality (number of particles). However, the diagnosis of those data needs more research for determining the structural health and lifetime prediction of wind turbines [11].

### 1.3 Problem statement

The problem that arises from the description of the current lifetime prediction is the unknown load on a wind turbine. Because the load is unknown, statistics are currently used to predict the wind load and lifetime of components. In practise, the lifetime of real components differs from the prediction. This difference results in unexpected component failures, which are very costly. A more sophisticated but low cost approach is needed to improve the lifetime prediction of wind turbine components [15].

### 1.4 Research questions

The goal of this research is to define a structural dynamic model to describe the relation between measured vibrations and the internal loads. The failure model of components about wear and fatigue is assumed to be known, for example given by bearing and gearbox manufacturers or design standards, requiring quantified loads as input. The research question is stated as:

*To what extent can internal forces, moments and torques of a wind turbine be determined, using accelerometers?*

The following sub questions are stated to split up the research question:

1. How can an analytic structural model be defined and applied to a wind turbine?
2. How can a numerical structural model be defined and applied to a wind turbine?
3. What manipulation is needed to use a structural model for measurement processing?
4. What is the accuracy of the structural model?

The first two sub questions are about describing the structural dynamic model. An analytic model is considered because it is expected to be fast and to give insight in the dynamical behaviour of the system. A numerical model is expected to be fast as well, but more geometric details may be added. The third sub question is about the interface between the accelerometers and the structural model. The last sub question is about the accuracy of the model. For a real wind turbine, the lifetime prediction has to be accurate over a lifespan of about twenty years [16]. An error of 10% in this time prediction is assumed to be acceptable, which is about two years. A critical component of a wind turbine is a bearing, where its lifetime is dependent on the load it carries. Its basic rating life is described by the  $L_{10}$  norm [17]:

$$L_{10} = \left( \frac{C}{P} \right)^p \quad (1.1)$$

Where

$L_{10}$  = basic rating life (at 90%) reliability, millions of revolutions

$C$  = basic dynamic load rating from bearing geometry, N

$P$  = equivalent dynamic bearing load, N

$p$  = exponent for the life equation, 3 for ball bearings or 10/3 for roller bearings

As can be seen, allowing an 10% error of  $L_{10}$  results in an allowed error for  $P$  in ball bearings of 2.15%. The lifetime model of other critical components is assumed similar to the  $L_{10}$  norm. Therefore, the accuracy of the load prediction is required to be within 2.15% error.

### 1.5 Approach

A mechanical model can be used to determine internal loads and remaining lifetime. This is similar to the approach showed in figure 1.2, but without the statistic prediction. The wind speed and turbulences are the input of the system. Usage is determined by the user, which is in many cases the manufacturer or operator by a (remote) control system. This causes loads on the

mechanical system, resulting in a remaining lifetime. To quantify it, a structural model can be used to determine these mechanical loads on components, for example bearings. These internal loads are used as input for fatigue models. In this case wear and fatigue are assumed the most dominant. This results in a damage accumulation which can be used for setting up a maintenance strategy to avoid failures. Preferably, the loads on the system are directly known and used as input for the mechanical model to determine internal loads. However, it is not possible to measure loads, such as forces and torques, on the wind turbine directly, since the usage by wind and turbulence is not exactly known. Therefore the loads need to be deduced from measurable parameters, such as the relative displacement of components caused by these loads. Nonetheless, relative displacements cannot be measured in a wind turbine [18]. As stated before, accelerometers are already used and trusted during operation by CMS. From an economical view, using this sensors is advantageous above using expensive new measurement equipment. Preferably, the CMS sensors should be used as input in the model. If an harmonic excitation is assumed, the acceleration sensors move with a periodic motion. Therefore the dynamic displacements can be predicted accurately from the accelerations, since the noise offset can be easily removed [19]. The drawback of using accelerations as input is the disregarded static displacement offset. The structural model should be preferably analytic to make it fast in calculations and give insight in external and internal dynamics of the system. A fast calculation of the lifetime is required to process the data during operation. Bending of a structure can be described by its bending modes. These depend on the excitation frequency. This implies frequency dependent displacements, which should be present in the structural dynamic model. The periodic excitation is due to the unequal wind load on the separate blades during rotation, since the wind speed is higher at more height from the ground [20].

The overview with the relation between usage and lifetime is partly modified and can be seen in figure 1.4, which is an modification to figure 1.2 with a change between usage and determining the internal loads. Since a wind turbine has many components, only the most critical are con-

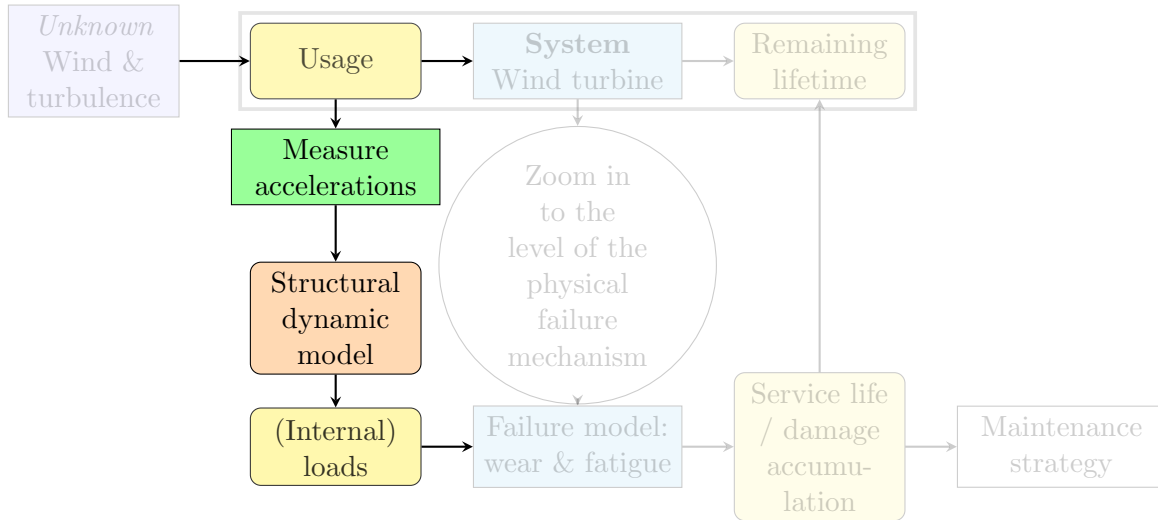


Figure 1.4: Preferred model using CMS accelerometers, modified part of lifetime prediction in figure 1.2, adapted from [4].

sidered. These are defined as the drive train and the rotor blades, based on relative failure rates and maintenance costs [21]. The aerodynamic load calculation of the rotor depends on, among others, blade design details, lift and drag values, angle of attack (pitch angle), wind speed (at different heights and including turbulences), side and shear winds and yaw misalignment [22]. These are almost all related to the field of fluid and aero dynamics. For the drive train only the vibration response during excitation is needed. The vibration response includes all fluctuations and effects. This is related to the field of (multi body) dynamics. To focus in depth on a small specific part of the critical components concerning dynamics, this research will focus on the wind turbine drive train.

## 1.6 Drive train configuration

Wind turbine drive trains are available in different configurations, the considered ones can be seen in figure 1.5. A short description is given below.

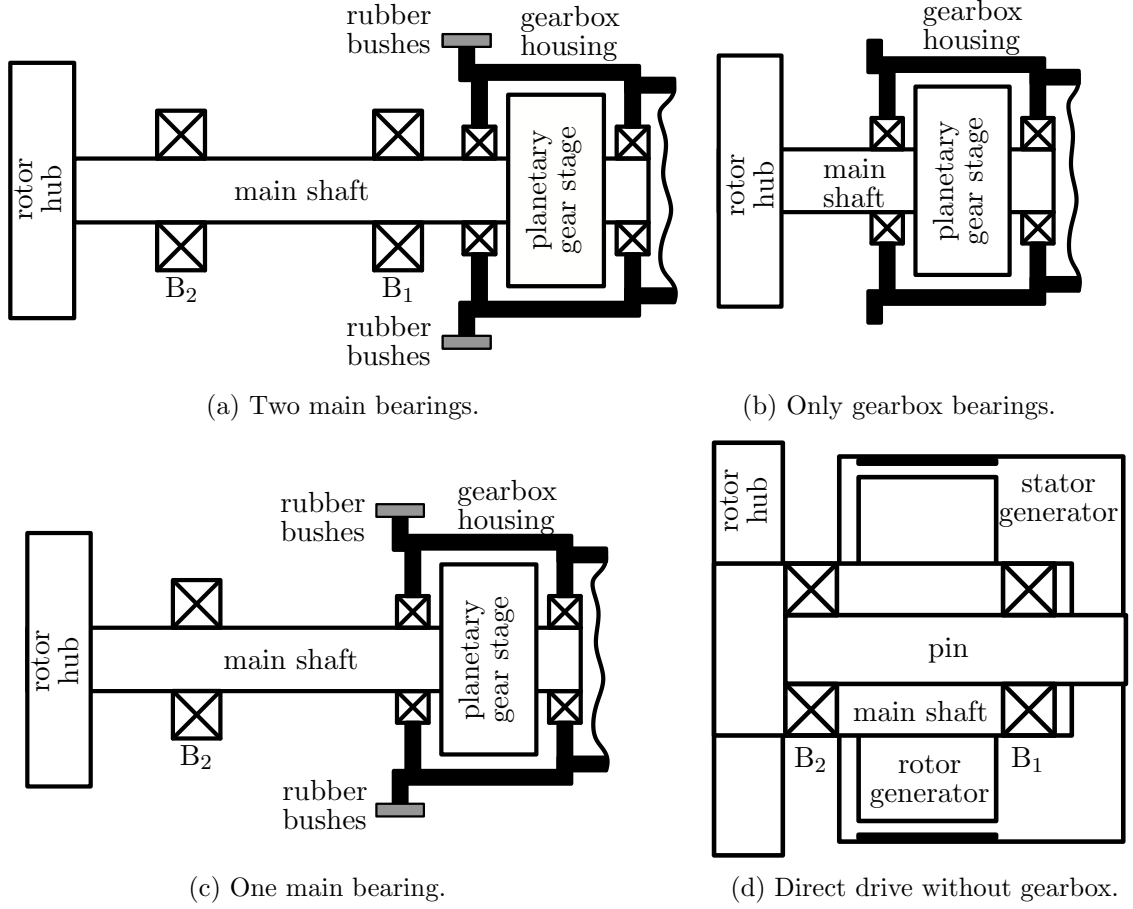


Figure 1.5: Schematic overviews with different drive train configurations, adopted from [18].

The different configurations in figure 1.5 are explained by Rommel [18].

- (a) Two main bearings, two gearbox bearings and two rubber bushes support the moment of the gearbox [23]. Important to note is the over constraint by the rubber-bushes. Both the rotor and the gearbox are 'overhanging' weights.
- (b) Only two gearbox bearings. The rotor is an overhanging weight, the gearbox is placed between the bearings. The differences between figure 1.5a are the two removed main bearings. The gearbox housing is fixed to the base frame.
- (c) One main bearing in combination with the gearbox bearings and rubber bushes. This is a combination between the first two mentioned configurations, but with only one main bearing removed from figure 1.5a.
- (d) The direct drive. It is similar to figure 1.5b, but instead of the gearbox a low speed generator is placed between the bearings. Because of the low speed generator, no mechanical speed transmission is needed [24]. The differences between figure 1.5a are the two removed main bearings.

Figures 1.5b, 1.5c, 1.5d are simplified configurations of figure 1.5a. For example by using no or one main bearing. Also, figure 1.5a has the constrained forces due to the rubber bushes. Because of these two reasons, this research will focus on the configuration with two main bearings.

## 1.7 Test bench

Since no acceleration data, geometries and properties of a real wind turbine are available a test bench with known geometries and properties will be used as feasibility study to the dynamics of a wind turbine drive train. This section gives a description of the test bench and explains the excitation rotor force. Some short justifications to exclude stiffness and damping effects of shafts dependent on the rotating frequency. The shafts can be modelled as beams if the speed influence on the damping and stiffness of the shaft can be neglected.

### 1.7.1 Description

Figure 1.6 shows a CAD model of the test bench. The test bench consists of a flexible base frame with a rotating flexible shaft, gearbox and generator. The rotor is modelled as rotating unbalanced mass. A faster rotor speed will be used in the range between 3.0 Hz and 8.0 Hz compared to the relative slow speed about 15 RPM of a real wind turbine. This speed is to excite the first four resonance frequencies for  $z$ -bending and shaft torsion. Another practical reason for this frequency range are the available accelerometers. A detailed CAD model and used dimensions can be found in appendix A.

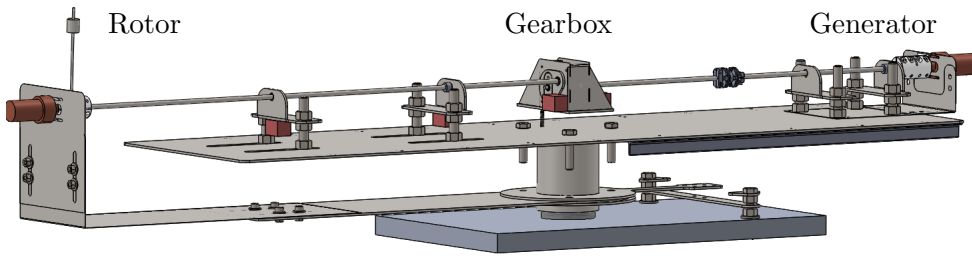


Figure 1.6: CAD model test bench 3D view, *in corporation with D. Berendsen.*

### 1.7.2 Excitation force

Figure 1.7 shows a schematic overview of the rotor, which is modelled as a rotating unbalance to mimic the harmonic wind load variation. The 'rotor' is mounted to the Low Speed Shaft (LSS), shown as blue dot. The rotating unbalance with speed  $\Omega$  results in force in  $z$ -direction  $F_{R,z}$ , force in  $y$ -direction  $F_{R,y}$  and fluctuating torque  $T_R$  around the  $z$ -axis. Because of the rotating unbalance mass  $m_u$  with radius  $r_u$ , the force in  $z$ -direction  $F_{R,z}$  and torque at the shaft  $T_R$  are described by:

$$F_{R,z}(t) = m_u(r_u\Omega^2 \sin(\Omega t) - \ddot{z}(t)) \quad (1.2)$$

$$T_R(t) = m_u r_u g \cos(\Omega t) \quad (1.3)$$

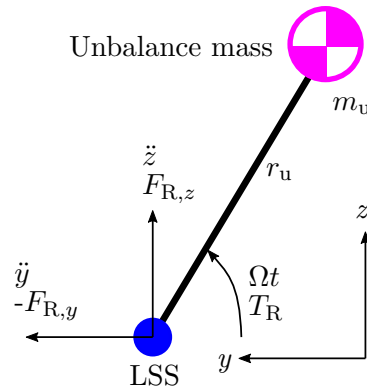


Figure 1.7: Free body diagram of the rotor, represented by a rotating mass, YZ view.

Only forces and displacements in  $z$ -direction are considered in this research. The stiffness of the base frame in  $y$ -direction is much stiffer compared to the  $z$ -direction based on the rectangular area inertia. The stiffness for the shaft is the same in  $z$ - and  $y$ -direction, because of the circular cross-section. Shaft modeshapes for both directions are assumed to be similar.



### 1.7.3 Rotary inertia effect for rotating shafts

An analytical derivation of the equation of motion for a rotating beam is given to determine the rotary and gyroscopic effects. The equations of motion for a circular beam with rotatory inertia according to [25] are given by:

$$\frac{\partial Q_z}{\partial x} = \rho A \frac{\partial^2 w_z}{\partial t^2} \quad (1.4)$$

$$EI \frac{\partial^3 w_z}{\partial x^3} + Q_z = \rho I \frac{\partial}{\partial x} \frac{\partial^2 w_z}{\partial t^2} + 2\Omega \rho I \frac{\partial}{\partial x} \frac{\partial w_y}{\partial t} \quad (1.5)$$

where

$A$  = cross sectional area,  $\text{m}^2$

$E$  = Young's modulus,  $\text{N m}^{-2}$

$I$  = area inertia,  $\text{m}^4$

$Q$  = shear force,  $\text{N}$

$t$  = time,  $\text{s}$

$w$  = radial deflection,  $\text{m}$

$\rho$  = density,  $\text{kg m}^{-3}$

$\Omega$  = rotational speed,  $\text{rad s}^{-1}$

The force and moment balances for an infinitesimally thin shaft segment are visualized in figure 1.8.

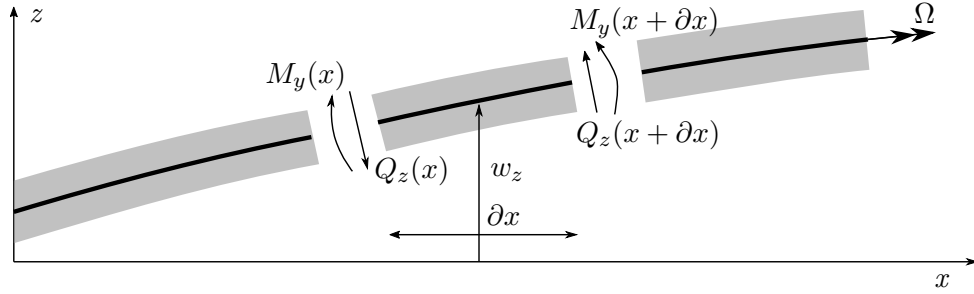


Figure 1.8: An infinitesimal rotating shaft segment, adapted from [25]

By eliminating shear forces choosing radial displacement  $z$  as complex quantity of  $w_z$  and  $w_y$ :

$$z = w_z + iw_y \quad (1.6)$$

The following equation of motion for a rotating shaft is obtained:

$$EI \frac{\partial^4 z}{\partial x^4} - \rho I \left( \frac{\partial^4 z}{\partial x^2 \partial t^2} - 2i\Omega \frac{\partial^3 z}{\partial t \partial x^2} \right) + \rho A \frac{\partial^2 z}{\partial t^2} = 0 \quad (1.7)$$

For a hinged-hinged shaft with zero displacement and moment at the ends with length  $L$  the boundary conditions are given by:

$$z(0, t) = z(L, t) = 0 \quad (1.8)$$

$$\frac{\partial^2 z(0, t)}{\partial x^2} = \frac{\partial^2 z(L, t)}{\partial x^2} = 0 \quad (1.9)$$

A common trial function for  $z$  is used:

$$z = Z \sin\left(\frac{\pi n x}{L}\right) e^{i\omega t} \quad (1.10)$$

where  $n$  is the Eigenmode number and  $Z$  the spatial amplitude. Applying this trial function and solving for the Eigenfrequency results in:

$$\left[ 1 + \frac{\pi^2 n^2 I}{AL^2} \left( 1 - 2\frac{\Omega}{\omega} \right) \right] \omega^2 - \frac{EI}{\rho A} \frac{\pi^4 n^4}{L^4} = 0 \quad (1.11)$$

The following non-dimensional parameters factor  $\mu$  and non-dimensional radius of gyration  $r'$  can be used:

$$\mu = \left( \frac{\omega_c}{\omega} \right)^2 \quad (1.12)$$

$$\omega_c = \frac{n^2 \pi^2}{L^2} \sqrt{\frac{EI}{\rho A}} \quad (1.13)$$

$$r' = \sqrt{\frac{I}{AL^2}} \quad (1.14)$$

where  $\omega_c$  is the analytical solution for a non rotating hinged-hinged beam, corresponding to [26]. Using equation 1.11 factor  $\mu$  can be expressed as:

$$\mu = \left[ 1 + (\pi n r')^2 \left( 1 - \frac{2\Omega}{\omega} \right) \right] \quad (1.15)$$

For the test bench shafts with a shaft radius of 3.0 mm and a shaft length of 200 mm  $r'$  is negligible small. Therefore the shaft eigenfrequencies are assumed not affected by rotary or gyroscopic effects. In the next section the rotary effects on the rotor unbalance are determined.

#### 1.7.4 Rotary effects at the rotor

A fast spinning shaft or rotor has a stabilizing effect. This is known as gyroscopic precession. A small study to rotating components of the test bench is done to verify this effect. The rotor with unbalance is assumed sensitive to it, because the rotor has a relatively heavy rotating mass on a long, slender shaft of the test bench. This is shown in figure 1.9, at a maximum deflection and rotation of the rotor  $\delta$  and  $\theta$ , respectively. The rotor consists of a coupling with  $m_R$  and inertia  $J_R$ . The rotor is an unbalanced mass with radius  $r_u$  and mass  $m_u$ . Bearing  $B_2$  is located on the right.

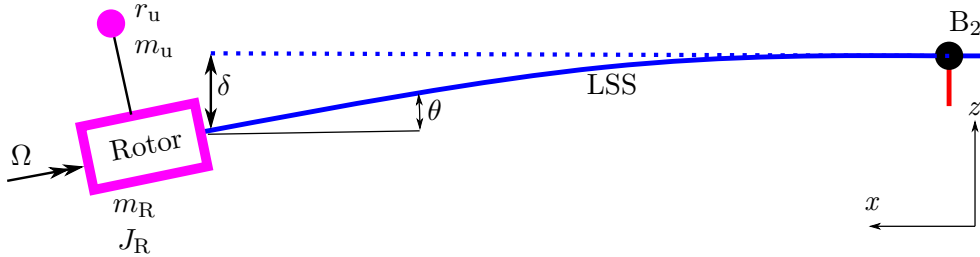


Figure 1.9: Schematic overview rotor with rotating unbalance, deformed LSS, XZ view.

To determine the effect of gyroscopic precession on the rotor and LSS a simplification to a rotating clamped beam is made, as can be seen in figure 1.10. The force and gyroscopic moment due to the gyroscopic precession are indicated by  $F_{R,z}$  and  $M_y$ , respectively. This approach is adapted from Tiwari [27]. The rotor coupling is modelled as rigid disc with mass  $m_d$  and inertia  $J_d$ . The LSS rotates with speed  $\Omega$ , has stiffness properties  $EI$  and length  $l$ . Its mass is in this case assumed significantly smaller compared to the rotor mass. Bearing  $B_2$  is assumed fixed.

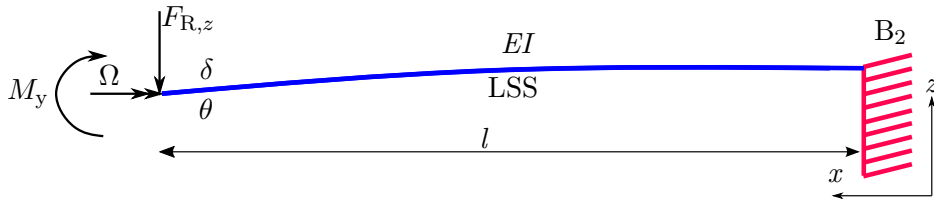


Figure 1.10: Free body diagram of the rotor and part of LSS, XZ view.

Force  $F_{R,z}$  is due to the unbalanced mass and rotation speed  $\omega$  of the rotor around offset  $\delta$  with centrifugal acceleration:

$$F_{R,z} = m_R \Omega^2 \delta + m_u \Omega^2 (r_u + \delta) \quad (1.16)$$

The moment  $M_y$  is due to gyroscopic precession [28]:

$$M_y = \Omega^2 J_R \theta \quad (1.17)$$

The displacement and rotation are given by the beam bending theory:

$$\delta = \frac{F_{R,z} l^3}{3EI} - \frac{M_y l^2}{2EI} \quad (1.18)$$

$$\theta = \frac{F_{R,z} l^2}{2EI} - \frac{M_y l}{EI} \quad (1.19)$$

It is assumed that the gyroscopic precession is of significant effect if it compensates the force  $F_z$ , so when  $\delta$  and  $\theta$  are zero. Solving for zero deflection and rotation results in a critical shaft speed  $\Omega_{cr}$  of 17.8 Hz, with:

$E$  = E-modulus for steel, 210 GPa

$I$  = area inertia LSS cross section,  $6.9 \times 10^{-11} \text{ m}^4$

$m_R$  = mass rotating rotor coupling, 0.175 kg

$J_R$  = mass inertia rotating rotor coupling,  $2.0 \times 10^{-5} \text{ kg m}^2$

$l$  = length LSS, 250 mm

$r_u$  = radius unbalance, 10 mm

$m_u$  = mass unbalance, 48 g

As was shown, at speeds from 17.8 Hz the gyroscopic effect is of significant influence. Therefore, the gyroscopic effect is neglected for lower speeds.



## 2 Methodology

The rotating unbalance at the test bench, described in section 1.7, causes harmonic vibrations. These vibrations can be measured with accelerometers, located at specific locations of the base and gearbox. The choice where to put the sensors is limited, because they cannot be put on the rotating shaft due to wiring. Further, a structural model is needed to process these accelerations and predict internal loads, for example in the bearings. This chapter describes three different structural models: an analytic model, a Spacar model and a manually defined FEM model.

### 2.1 Analytic structural model

An analytic approach to describe the dynamics of the test bench is considered in this section, because this approach gives insight in the dynamic behaviour and gives exact solutions without time consuming iterations or integration. The derivations in this section are based on the dictaat Dynamics 2 [26]. In general, an analytical model is faster in calculation compared to a numerical one, which is advantageous for a model to use during operation. To describe the response of a flexible structure to an harmonic load, the modeshapes of the structure are needed. First these modeshapes are determined as Eigenvalue problem. Second these modeshapes have to be scaled in order to use them describing an harmonic forced vibration.

#### 2.1.1 Modeshapes

The equation of motion for transverse vibrations in a beam (Euler-Bernoulli) is given in equation 2.1. This holds for example for a shaft element of the test bench.

$$\rho A \frac{\partial^2 w(x, t)}{\partial t^2} + EI \frac{\partial^4 w(x, t)}{\partial x^4} = f(x, t) \quad (2.1)$$

With  $\rho$  the density,  $A$  the cross sectional area,  $E$  the Young's modulus and  $I$  the area moment of inertia around the  $y$ -axis. Function  $w(x, t)$  describes the  $z$ -displacement as function of location and time. A schematic overview with these parameters can be seen in figure 2.1. In this case, the cross section is chosen circular for a shaft, shown at the right side.

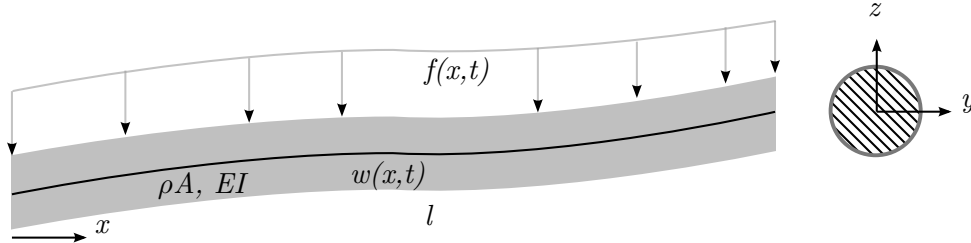


Figure 2.1: Schematic overview analytic beam element, with side- and cross sectional view.

Using separation of variables of  $w(x, t) = W(x)T(t)$  and  $f(x, t) = 0$  for free vibrations of the homogeneous solution with a constant cross section results in:

$$\frac{1}{T(t)} \frac{dT^2(t)}{dt^2} = -\frac{EI}{\rho A W(x)} \frac{d^4 W(x)}{dx^4} = -\omega^2 \quad (2.2)$$

Where  $\omega$  is the Eigenfrequency. This equation can be split in a transient and spatial part, resulting in the following differential equations:

$$\frac{d^2 T(t)}{dt^2} + \omega^2 T(t) = 0 \quad (2.3)$$

$$\frac{d^4 W(x)}{dx^4} - \beta^4 W(x) = 0, \quad \beta^4 = \frac{\rho A \omega^2}{EI} \quad (2.4)$$

Where  $\beta$  is called the wave number. As can be seen,  $\beta$  depends on the geometry and material and is different for each individual beam. A solution for the spatial differential equation of amplitude

$W(x)$  a beam is given by:

$$W(x) = B_1 \cos(\beta x) + B_2 \sin(\beta x) + B_3 \cosh(\beta x) + B_4 \sinh(\beta x) \quad (2.5)$$

These can be differentiated resulting in expressions for:

- Angle  $\theta(x) = W'(x)$
- Moment  $M_y(x) = EIW''(x)$
- Shear force  $Q(x) = EIW'''(x)$

Where superscript ' denotes a differentiation w.r.t.  $x$ . Each beam element needs four boundary conditions (BCs), since equation 2.4 is a fourth order equation. Defining them in matrix vector form results in matrix  $\mathbf{D}$  with cos, sin, sinh and cosh values depending on  $\beta$  (indirect on  $\omega$ ) and vector  $\mathbf{B}$  with the scaling values  $B_1$  till  $B_4$  for each beam:

$$[\mathbf{D}(\omega)] \{\mathbf{B}\} = \mathbf{0} \quad (2.6)$$

Matrix  $\mathbf{D}$  is a square matrix with size four times the amount of beams, dependent on frequency  $\omega$ . The determinant  $|\mathbf{D}(\omega)| = 0$  for resonance frequencies  $\omega_n$  is solved numerically, since for more than one element, the analytic solution does not exist. Inserting  $\omega_n$  back in equation 2.6 results in the Eigenvectors (or modeshapes) of the system  $\alpha_s W(\omega, x)$ . In this,  $\alpha_s$  is still undetermined. A method to determine the scaling factor is described in the next section.

### 2.1.2 Modeshape scaling

Modeshape scaling is needed, because scaled modeshapes can describe the response of the beam to an harmonic load. The scaling is done for one clamped beam element (left side) and a free-end (right side), as is shown in figure 2.2. The four boundary conditions at both the beam ends are given, as derivations from equation 2.3 and 2.5.

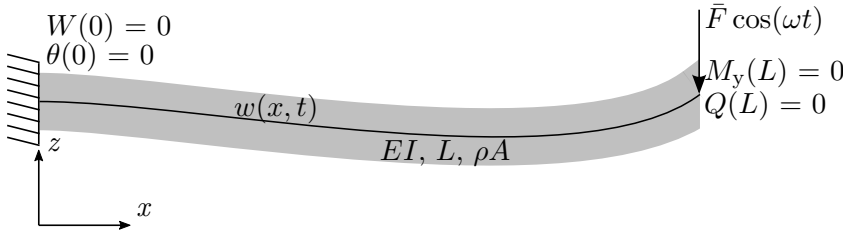


Figure 2.2: Free body diagram of an analytic clamped-free beam with harmonic excitation,  $XZ$  view.

Using the spatial part  $W(x)$ , two distinct frequencies  $\omega_i$  and  $\omega_j$  and their corresponding modeshapes  $W_i(x)$  and  $W_j(x)$ , for a beam without point mass at the free end:

$$EI \frac{d^4 W_i(x)}{dx^4} = \omega_i^2 \rho A W_i(x) \quad (2.7)$$

$$EI \frac{d^4 W_j(x)}{dx^4} = \omega_j^2 \rho A W_j(x) \quad (2.8)$$

The first equation is multiplied with  $W_j(x)$  and integrated over the beam length  $L$ :

$$EI \int_0^L W_j(x) \frac{d^4 W_i(x)}{dx^4} dx = \omega_i^2 \rho A \int_0^L W_i(x) W_j(x) dx \quad (2.9)$$

Using integration by parts the left hand side can be split up in different integrals:

$$\begin{aligned} EI \left[ W_j(x) \frac{d^3 W_i(x)}{dx^3} \right]_0^L - EI \left[ \frac{dW_j(x)}{dx} \frac{d^2 W_i(x)}{dx^2} \right]_0^L + EI \int_0^L \frac{d^2 W_i(x)}{dx^2} \frac{d^2 W_j(x)}{dx^2} dx \\ = \omega_i^2 \rho A \int_0^L W_i(x) W_j(x) dx \end{aligned} \quad (2.10)$$

For geometrical or natural boundary conditions, for example clamped, simply supported (hinged) or a free end, the terms between square brackets are always zero by the combination of displacement-shear force and angle-moment at the beam end boundaries:

- Clamped end:  $W = 0$  and  $\frac{dW(x)}{dx} = 0$
- Hinged end :  $W = 0$  and  $\frac{d^2W(x)}{dx^2} = 0$
- Free end:  $\frac{d^3W(x)}{dx^3} = 0$  and  $\frac{d^2W(x)}{dx^2} = 0$

The same integration and multiplication with  $W_i(x)$  can be applied to the second equation of 2.7. This results in a formulation with the same left hand side as 2.10. This can only be true if the following holds for two distinct modeshapes:

$$\rho A \int_0^L W_i(x) W_j(x) dx = \delta_{ij} \quad (2.11)$$

Where  $\delta_{ij}$  is the Kronecker delta. Note, both modeshapes  $W_i$  and  $W_j$  still depend on scaling factor  $\alpha_s$ .

Similar to the beam with free-end, the condition for adding point mass  $m$  and inertia  $J$  at the free end of the beam can be derived, resulting in:

$$\rho A \int_0^L W_i(x) W_j(x) dx + m W_i(L) W_j(L) + J W_i'(L) W_j'(L) = \delta_{ij} \quad (2.12)$$

Now, scaling factor  $\alpha_s$  in both  $W_i$  and  $W_j$  can be determined. Note, this holds for only one beam element. As can be seen, the scaling factor formulation increases rapidly in complexity by adding more details like point masses.

### 2.1.3 Harmonic forced vibration

With the modeshapes determined and scaled, the relation between an harmonic load and displacement of a beam can be determined. For the forced vibration, consider the beam equation 2.1. The response of a beam can be described as the linear combination of several modeshapes multiplied with a transient function:

$$w(x, t) = \sum_{i=1}^{\infty} W_i(x) \eta_i(t) \quad (2.13)$$

Substitution in equation 2.1, multiplying with  $W_j(x)$  and integrating over the length  $L$  of the beam yields:

$$\sum_{i=1}^{\infty} \left[ \int_0^L \rho A W_i(x) W_j(x) dx \right] \frac{d^2 \eta_i(t)}{dt^2} + \sum_{i=1}^{\infty} \left[ \int_0^L E I W_j(x) \frac{d^4 W_i(x)}{dx^4} dx \right] \eta_i(t) = \int_0^L W_j(x) f(x, t) dx \quad (2.14)$$

Because of the orthogonality conditions this formulation can be normalized. This is similar to the normalization of a 2 DoF system and results in:

$$\frac{d^2 \eta_i(t)}{dt^2} + \omega_i^2 \eta_i(t) = Q_i(t) \quad (2.15)$$

An harmonic force  $f(x, t)$  at the beam end is assumed, as was shown in figure 2.2:

$$f(x, t) = \bar{F} \cos(\omega t) \quad (2.16)$$

Using this harmonic load as load vector  $Q_i(t)$  at the right side of equation 2.14:

$$Q_i(t) = \int_0^L W_j(x) \bar{F} \cos(\omega t) dx = F_i \cos(\omega t) \quad (2.17)$$

Because of the harmonic excitation the steady state solution for  $\eta_i$  is:

$$\eta_i(t) = \frac{\bar{F}}{\omega_i^2 - \omega^2} \cos(\omega t) \quad (2.18)$$

At resonance frequencies, where  $\omega = \omega_i$ , the solution for the transient part is infinite. The reason for this is the lack of damping. Combining the spatial and transient part results in a function for a point at the beam at a certain time and location:

$$w(x, t) = \sum_{n=1}^{\infty} W_n(x) \frac{\bar{F}}{\omega_n^2 - \omega^2} \cos(\omega t) \quad (2.19)$$

As can be seen, an infinite amount of modeshapes is summed, but the influence of a modeshape decreases quadratic with the frequency. In practice a finite amount of modeshapes is taken into account based on results.

Equation 2.19 can be reversed to get the force  $\bar{F}$  as function of the displacement  $w(x, t)$ . However, for simple geometry it is already a fairly time consuming and complicated process [29]. Determining scaling factor  $\alpha_s$  for multiple connected beams will be even more complicated due to the cross terms between separate beam modeshapes, masses and inertia.

Another disadvantage is the complex damping phenomenon, which is excluded in this analytic approach [29]. Especially at Eigenfrequencies, damping is relevant, as was shown in equation 2.18.

So although the analytical solution is defined simply, computational fast and giving insight in the dynamical behaviour of flexible beams, the usage is limited to a single, undamped beam. Using multiple beam elements results in a complex formulation.

## 2.2 FEM structural model

In this section a structural model will be described by using the finite element method (FEM). Compared with the analytic approach, a more complex model with multiple beams including damping can be defined with FEM. As stated as well for the analytic model, the FEM model should be fast in order to process acceleration data real time. Several FEM programs are available to build a structural model and perform load calculations, for example Ansys or Spacar. The use of Spacar is preferred because of its simplicity in defining and calculating a FEM model. However, these FEM programs have a disadvantage; details of the structural model, such as the gearbox ratio, can not be added to the structural model. Therefore, FEM is also programmed manually with those details. Both FEM approaches are considered to compare and verify results and show significance of those details.

### 2.2.1 Spacar

Spacar is a FEM program developed at the University of Twente [30] and is based on Matlab. With use of the extended version, the geometry can be defined and run in Spacar, which is advantageous for fast checking or optimizing of designed geometries. A simple definition and a fast calculation are required for the structural model.

A beam can be defined by its cross sectional area and inertia from coordinate  $p$  to  $q$  in 3D, as can be seen in figure 2.3. Beams can be coupled by displacement or rotation. The first two deformations of a beam are elongation and torsion, respectively  $\epsilon_1$  and  $\epsilon_2$ . Spacar uses a different definition of coordinate displacements and rotations  $\epsilon_3$ ,  $\epsilon_4$ ,  $\epsilon_5$  and  $\epsilon_6$  compared to other FEM programs. Other FEM programs use the displacement and rotation of a node, as will be described in section 2.2.2. In general, the different definition of bending modes makes it difficult to export or manipulate the structural model. Exporting and manipulation of the model is necessary for processing acceleration data. Therefore, Spacar is only used to verify the modeshapes of the manually defined FEM.

### 2.2.2 Manual program

Manually describing a FEM model has a couple of advantages: It gives insight in the FEM structure and linking between elements and boundary conditions. Also, the structure can be built by simple beams, enabling a fast computation. The main advantage is the option to add extra details, for example the gearbox ratio. This section describes the used theory and is based on [32, 33]. First an overview of the FEM describing beam elements is given. Second the



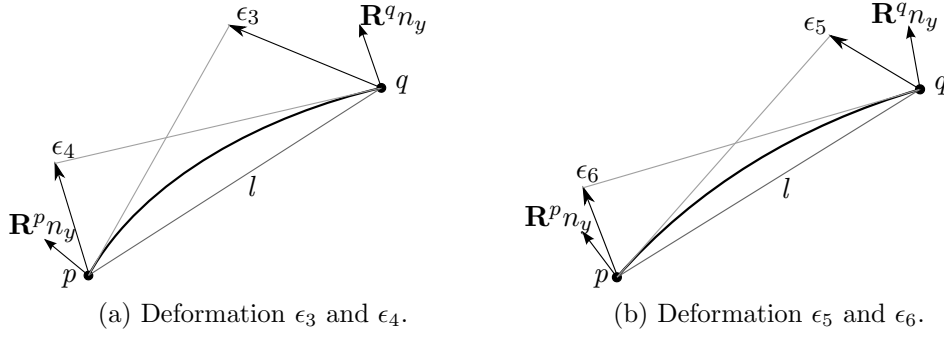


Figure 2.3: Schematic overview Spacar beam with bending deformation coordinates, adapted from [31].

Lagrange multiplier theorem is explained, which can be used to link beam elements together or add geometrical constraints. Third damping of a FEM system is explained, which is relevant at resonance frequencies.

### FEM in general

Consider the following dynamic system:

$$\mathbf{M}\ddot{\mathbf{q}}(t) + \mathbf{C}\dot{\mathbf{q}}(t) + \mathbf{K}\mathbf{q}(t) = \mathbf{R}(t) \quad (2.20)$$

With mass matrix  $\mathbf{M}$ , acceleration vector  $\ddot{\mathbf{q}}(t)$ , damping matrix  $\mathbf{C}$ , velocity vector  $\dot{\mathbf{q}}(t)$ , stiffness matrix  $\mathbf{K}$ , displacement vector  $\mathbf{q}(t)$  and load vector  $\mathbf{R}$ , where the vectors contain translations and rotations. An harmonic displacement and excitation with frequency  $\Omega$  can be described in the time domain by:

$$\mathbf{q}(t) = \bar{\mathbf{q}}e^{i\Omega t} \quad (2.21)$$

$$\mathbf{R}(t) = \bar{\mathbf{R}}e^{i\Omega t} \quad (2.22)$$

where  $\bar{\mathbf{q}}$  and  $\bar{\mathbf{R}}$  are the amplitude of the displacement and force, respectively. Vector  $\mathbf{q}(t)$  can be differentiated to velocities  $\dot{\mathbf{q}}(t)$  and accelerations  $\ddot{\mathbf{q}}(t)$ :

$$\dot{\mathbf{q}}(t) = i\Omega\bar{\mathbf{q}}e^{i\Omega t} = i\Omega\mathbf{q}(t) \quad (2.23)$$

$$\ddot{\mathbf{q}}(t) = -\Omega^2\bar{\mathbf{q}}e^{i\Omega t} = -\Omega^2\mathbf{q}(t) \quad (2.24)$$

For a known acceleration the displacement can be determined by reverting equation 2.24, (similar to equation 2.3), which is needed as input for the FEM program. This displacement is much more accurate in comparison to twice integrating the acceleration, since that has a minimal error of about 9% [34]. Applying these velocity and acceleration to equation 2.20 results for the spatial part in:

$$[-\Omega^2\mathbf{M} + i\Omega\mathbf{C} + \mathbf{K}]\bar{\mathbf{q}} = \bar{\mathbf{R}} \quad (2.25)$$

This holds for a general harmonic frequency. Because FEM beams are assumed to have a linear stiffness, results from higher harmonics can be added. This is for example the case for the higher harmonics caused by the three blades of a wind turbine [18]. A beam element with bending and torsion between node  $i$  and  $j$ , has six degrees of freedom  $\mathbf{q}$ , all time dependent:

$$\mathbf{q} = [z_i, \theta_i, \psi_i, z_j, \theta_j, \psi_j]^T \quad (2.26)$$

Where  $z$  is a displacement in  $z$ -direction,  $\theta$  a rotation around the  $y$ -axis and  $\psi$  a rotation around the  $x$ -axis. Tension in axial direction is neglected, since the stiffness in this direction is much higher in comparison with other directions. The beam with coordinates and used parameters is shown in figure 2.4. Load vector  $\mathbf{R}$  consists of:

$$\mathbf{R} = [F_i, M_i, T_i, F_j, M_j, T_j]^T \quad (2.27)$$

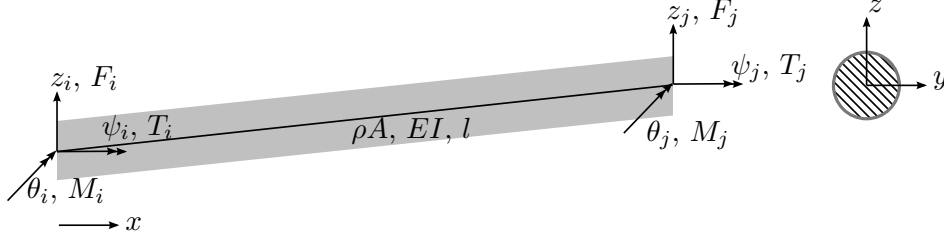


Figure 2.4: Schematic overview FEM beam element with nodes  $i$  and  $j$  with degrees of freedom  $\mathbf{q}$  and loads  $\mathbf{R}$ .

Where  $F$  is a force in  $z$ -direction,  $M$  a bending moment around the  $y$ -axis and  $T$  a torque around the  $x$ -axis. The stiffness and mass matrices  $\mathbf{K}$  and  $\mathbf{M}$  describing the relation between  $\mathbf{q}$  and  $\mathbf{R}$  are given by the Bernoulli-Euler and St. Venant theories. The Bernoulli-Euler beam theory is used to describe bending of the beams, where small, linear, deformations are assumed. For a beam element, this can be described by a 4x4 stiffness matrix applied to the displacement and angle of a node.

The St. Venant torsion theory is used to describe torsion in the beam elements, assuming small, linear deformations with a constant cross section and neglecting warping. This is described in 2x2 matrices. Both theories are combined, resulting in 6x6 stiffness and mass matrices. The shear modulus  $G$  is assumed  $E/3$ .

$$\mathbf{K} = \frac{E}{l} \begin{bmatrix} 12 \frac{I_y}{l^2} & 6 \frac{I_y}{l} & 0 & -12 \frac{I_y}{l^2} & 6 \frac{I_y}{l} & 0 \\ 6 \frac{I_y}{l} & 4I_y & 0 & -6 \frac{I_y}{l} & 2I_y & 0 \\ 0 & 0 & \frac{I_{yz}}{3} & 0 & 0 & -\frac{I_{yz}}{3} \\ -12 \frac{I_y}{l^2} & -6 \frac{I_y}{l} & 0 & 12 \frac{I_y}{l^2} & -6 \frac{I_y}{l} & 0 \\ 6 \frac{I_y}{l} & 2I_y & 0 & -6 \frac{I_y}{l} & 4I_y & 0 \\ 0 & 0 & \frac{I_{yz}}{3} & 0 & 0 & \frac{I_{yz}}{3} \end{bmatrix} \quad (2.28)$$

Where  $I_y$  is the area inertia around the  $y$ -axis,  $I_{yz}$  the area inertia of both the  $y$ - and  $z$ -axis and  $l$  the element length. The consistent mass matrix  $\mathbf{M}$  for one element with the masses distributed over the beam is described by:

$$\mathbf{M} = \frac{m}{2} \begin{bmatrix} \frac{156}{210} & \frac{221}{210} & 0 & \frac{54}{210} & \frac{-13l}{210} & 0 \\ \frac{221}{210} & \frac{4l^2}{210} & 0 & \frac{13l}{210} & \frac{-31l^2}{210} & 0 \\ 0 & 0 & \frac{r^2}{3} & 0 & 0 & \frac{r^2}{6} \\ \frac{54}{210} & \frac{13l}{210} & 0 & \frac{156}{210} & \frac{-22l}{210} & 0 \\ \frac{-13l}{210} & \frac{-31l^2}{210} & 0 & \frac{-22l}{210} & \frac{4l^2}{210} & 0 \\ 0 & 0 & \frac{r^2}{6} & 0 & 0 & \frac{r^2}{3} \end{bmatrix} \quad (2.29)$$

Where  $m$  is the beam element mass and  $r$  is the shaft radius. A lumped mass matrix  $\mathbf{M}_l$ , with the masses equally distributed at the two nodes, can be used for computational reasons:

$$\mathbf{M}_l = \frac{m}{2} \begin{bmatrix} 1 & 0 & 0 & 0 & 0 & 0 \\ 0 & \frac{1}{12}l^2 & 0 & 0 & 0 & 0 \\ 0 & 0 & \frac{r^2}{2} & 0 & 0 & 0 \\ 0 & 0 & 0 & 1 & 0 & 0 \\ 0 & 0 & 0 & 0 & \frac{1}{12}l^2 & 0 \\ 0 & 0 & 0 & 0 & 0 & \frac{r^2}{2} \end{bmatrix} \quad (2.30)$$

### Lagrange multipliers

For exact linking of beam coordinates the Lagrange multiplier theorem can be used, described in the multi-body dynamics approach from [33]. For example, this can be used to link the gearbox displacement and rotation to the shafts, where two nodes of two beam elements are merged.

The mass and stiffness matrices  $\mathbf{M}$  and  $\mathbf{K}$  for a constant frequency  $\Omega$  form the dynamic stiffness matrix  $\mathbf{A}$ :

$$\mathbf{A} = [\mathbf{K} - \Omega^2 \mathbf{M}] \quad (2.31)$$

The linking between two coordinates can be described by a constraint equation of motion  $\Phi$ . A direct linking between beams, for example the same  $z$ -displacement of nodes (node  $b$  has the same displacement as node  $a$ ), results in a constraint like:

$$a_z = b_z \quad (2.32)$$

Using a matrix vector notation results in a constraint equation  $\Phi = \mathbf{0}$ , with for the  $a$  and  $b$  indices:

$$\Phi = [1 \quad -1] \quad (2.33)$$

$\Phi$  with additional constraints for  $\mathbf{q}$  applied to the system of equations  $\mathbf{A} \cdot \mathbf{q} = \mathbf{R}$  holds:

$$\begin{bmatrix} \mathbf{A} & \Phi^T \\ \Phi & \mathbf{0} \end{bmatrix} \begin{Bmatrix} \mathbf{q} \\ \lambda \end{Bmatrix} = \begin{Bmatrix} \mathbf{R} \\ \gamma \end{Bmatrix} \quad (2.34)$$

Where the acceleration equation  $\gamma$  is given by:

$$\gamma = \Phi \ddot{\mathbf{q}} = -[\Phi \dot{\mathbf{q}}]_q \dot{\mathbf{q}} - 2\Phi_t \dot{\mathbf{q}} - \Phi_{tt} \quad (2.35)$$

Where subscript  $_q$  is a derivative w.r.t.  $q$  and subscript  $_t$  to time. As can be seen for constant constraints as in equation 2.34, the derivatives of  $[\Phi \dot{\mathbf{q}}]$  to  $\mathbf{q}$  and  $\Phi$  to  $t$  are zero for direct linking between elements, resulting in  $\gamma$  equals zero.

Part of the structural model validation is done using the modeshapes of the model. To solve for the modeshapes of the structural model, a reduction to only independent variables is needed. Some of  $q$  are dependent variables, since they are dependent (linked) to other nodes, for example, node  $b$  has the same displacement as node  $a$ . So the displacement of node  $b$  can be described by the displacement of node  $a$ , implying displacement  $b$  is dependent on displacement  $a$ . The system of equations in 2.34 can be rewritten (manipulated) to a dependent ( $d$ ) and independent ( $i$ ) part including the Lagrange multiplier  $\lambda$ , shown in equation 2.36.

$$\begin{bmatrix} \mathbf{A}_{dd} & \mathbf{A}_{di} & \Phi_d^T \\ \mathbf{A}_{id} & \mathbf{A}_{ii} & \Phi_i^T \\ \Phi_d & \Phi_i & \mathbf{0} \end{bmatrix} \begin{Bmatrix} \mathbf{q}_d \\ \mathbf{q}_i \\ \lambda \end{Bmatrix} = \begin{Bmatrix} \mathbf{R}_d \\ \mathbf{R}_i \\ \mathbf{0} \end{Bmatrix} \quad (2.36)$$

From this, the system can be manipulated to a reduced form with only independent variables, without dependent variables  $\mathbf{q}_d$  and Lagrange multiplier  $\lambda$ . Equation 2.31 can be reverted resulting in a system of equations which can be solved for the modeshapes:

$$[\hat{\mathbf{K}} - \Omega^2 \hat{\mathbf{M}}] \mathbf{q} = \hat{\mathbf{R}} \quad (2.37)$$

Where reduced mass matrix  $\hat{\mathbf{M}}$  is based on a transformation of the dependent and independent part of mass matrix  $\mathbf{M}$ :

$$\hat{\mathbf{M}} = \mathbf{M}_{ii} - \mathbf{M}_{id} \Phi_d^{-1} \Phi_i - \Phi_i^T \Phi_d^{-T} [\mathbf{M}_{di} - \mathbf{M}_{dd} \Phi_d^{-1} \Phi_i] \quad (2.38)$$

Where ' $T$ ' is the transpose of a matrix and ' $-T$ ' the inverse transpose. Because of the harmonic displacement assumption (equation 2.24), the same transformation also holds for the stiffness matrix  $K$ :

$$\hat{\mathbf{K}} = \mathbf{K}_{ii} - \mathbf{K}_{id} \Phi_d^{-1} \Phi_i - \Phi_i^T \Phi_d^{-T} [\mathbf{K}_{di} - \mathbf{K}_{dd} \Phi_d^{-1} \Phi_i] \quad (2.39)$$

Also load vector  $\mathbf{R}$  is reduced:

$$\hat{\mathbf{R}} = \mathbf{R}_i + \Phi_i^T \Phi_d^{-T} \mathbf{R}_d \quad (2.40)$$

As can be seen in equations 2.38, 2.39 and 2.40, the mass, stiffness and respectively load of the dependent variables  $\mathbf{q}_d$  is distributed over the remaining independent variables  $\mathbf{q}_i$  using the constraint equations  $\Phi$ . Now,  $\hat{\mathbf{K}}$  and  $\hat{\mathbf{M}}$  can be used to solve for the modeshapes.

## Damping

At resonance frequencies, the solution of an undamped system is infinite, as it is an Eigenvalue problem. To compensate for this, damping can be added. The most used damping approximation in FEM is Rayleigh damping, which assumes the damping proportional to the mass and stiffness matrix:

$$\mathbf{C} = [\alpha\mathbf{M} + \beta\mathbf{K}] \quad (2.41)$$

Where  $\alpha$  and  $\beta$  can be calculated from:

$$\zeta_i = \frac{\alpha}{2\omega_i} + \frac{\beta\omega_i}{2} \quad (2.42)$$

In case of rigid body motion it can not be applied, since damping would be infinite. Damping decreases with frequency [35]. Damping parameters  $\alpha$  and  $\beta$  are assumed to be constant and  $\zeta_i$  is the damping ratio of a resonance peak. In most real life structural applications mass damping is neglected [29], so  $\beta$  can be directly evaluated from  $\zeta$ . By the so called '3dB rule',  $\zeta$  can be estimated from experiments by measuring the width of a resonance peak [36], as can be seen in figure 2.5. The response of a multi degree of freedom system can be described by the contributions of single degree of freedom systems (SDoF). A SDof system with transfer function  $TF(s)$  with a certain Eigenfrequency  $\omega_n$  can be described in the Laplace domain  $s$  by:

$$TF(s) = \frac{\omega_n^2}{s^2 + 2\zeta\omega_n s + \omega_n^2} \quad (2.43)$$

Here,  $\omega_i$  is located at the maximum excitation  $\hat{a}$ . Note, a small frequency step is required to

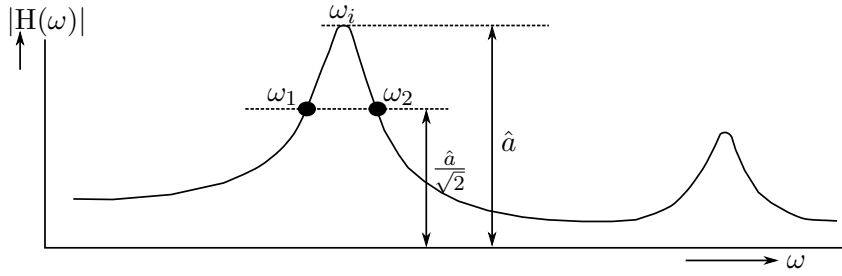


Figure 2.5: Schematic overview damping ratio estimation from amplitude resonance peak at frequency  $\omega_i$ , adapted from [36].

estimate the amplitude at  $\omega_1$  and  $\omega_2$  accurately. Damping ratio  $\zeta$  is given by [36]:

$$\zeta_i = \frac{\omega_2 - \omega_1}{2\omega_i} \quad (2.44)$$

From this, the damping parameter  $\beta$  can be evaluated using equation 2.42.

### 3 Application

In this chapter the discussed theory about the analytic, Spacar and the manual FEM approach will be applied to the test bench, which geometry is shown in appendix A. In all three structural models, the geometry of the test bench is simplified to beam elements in order to have a computationally fast model.

#### 3.1 Analytic

An analytic model of only the Base and LSS is made. This can be seen at the left half of the test bench in figure A.2. Only the LSS part of the test bench is taken into account for the structural modal, because the High Speed Shaft (HSS) part is stiffened and so has higher resonance frequencies. Figure 3.1 shows a schematic overview of the test bench modelled by analytic beams. Both the Base and LSS consist of three beam elements. The bearings (red line with black dot) are assumed rigid with inertia; the base (black) and LSS (blue line) have the same displacement at this node. At the LSS ends inertia (magenta dots) is added as rotor and gearbox (GB). A spring (grey) is added under the gearbox with stiffness  $k_{GB}$ . The DC motor driving the rotor is supported by a leafspring, which is shown also as grey spring with axial stiffness  $k_{RS}$ , connected to the ground. The Base is also connected to the ground by the rigid tower, shown as red square mark. Only bending in  $z$ -direction is considered. Each element

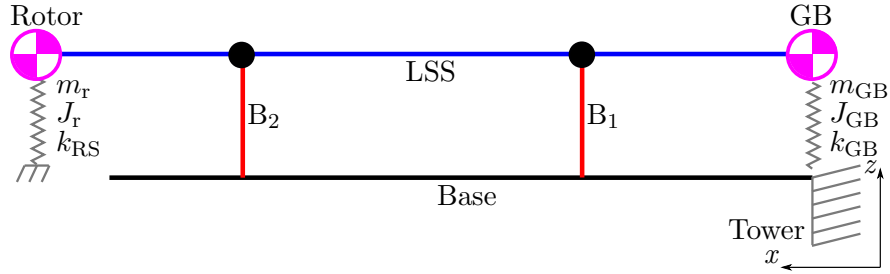


Figure 3.1: Schematic overview analytic model applied to the LSS part of the test bench, XZ view.

has four boundary conditions, for three base- and three shaft-elements this means 24 boundary conditions to solve for the Eigenfrequencies. The order of the boundary conditions starts at the tower to keep the matrix as sparse as possible for computational effort. The nodes are numbered as shown in figure 3.2. Each node has certain boundary conditions derived from equation 2.5, considering displacement  $W$ , angle  $\theta$ , bending moment  $M$  and shear force  $Q$ . The boundary conditions are listed in table 3.1.

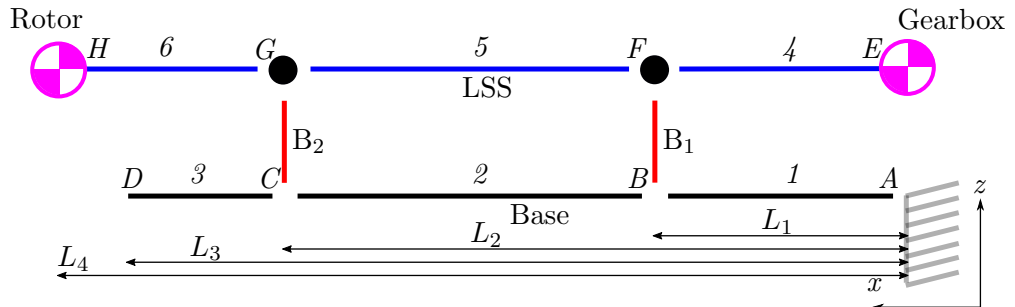


Figure 3.2: Schematic overview of the boundary conditions per node for the analytic model applied to the LSS part of the test bench.

Table 3.1: Boundary conditions analytic structural model ordered per node.

Node	Equation	Remarks
A	$W_1(0) = 0$ $\theta_1(0) = 0$	Clamped at tower
B	$W_1(L_1) = W_2(L_1)$ $\theta_1(L_1) = \theta_2(L_1)$ $M_1(L_1) = J_b \omega^2 \theta_1(L_1) + M_2(L_2)$ $Q_1(L_1) + m_b \omega^2 W_1 + Q_4(L_1) = Q_2(L_1) + Q_5(L_1)$	Continuous base displacement, angle, moment, shear force
C	$W_2(L_2) = W_3(L_2)$ $\theta_2(L_2) = \theta_3(L_2)$ $M_2(L_2) = J_b \omega^2 \theta_2(L_2) + M_3(L_2)$ $Q_2(L_2) + m_b \omega^2 W_2 + Q_5(L_2) = Q_3(L_2) + Q_6(L_2)$	Continuous base displacement, angle, moment, shear force
D	$M_3(L_3) = 0$ $Q_3(L_3) = 0$	Free end
E	$Q_4(0) - m_{GB} \omega^2 W_4(0) + k_{GB} W_4(0) = 0$ $M_4(0) + J_{GB} \omega^2 \theta_4(0) = 0$	Gearbox mass and inertia
F	$W_4(L_1) = W_5(L_1)$ $W_4(L_1) = W_1(L_1)$ $\theta_4(L_1) = \theta_4(L_1)$ $M_4(L_1) = M_5(L_1)$	Continuous shaft displacement, connection to base, angle, moment
G	$W_5(L_2) = W_6(L_2)$ $W_5(L_2) = W_2(L_2)$ $\theta_5(L_2) = \theta_5(L_2)$ $M_5(L_2) = M_6(L_2)$	Continuous shaft displacement, connection to base, angle, moment
H	$Q_6(L_4) - m_R \omega^2 W_6(L_4) + k_{RS} W_4(L_4) = 0$ $M_6(L_4) + J_R \omega^2 \theta_6(L_4) = 0$	Rotor mass and support stiffness rotor inertia

At node *A*, the structure is clamped to the tower. At nodes *B*, *C*, *F* and *G* the Base or LSS, respectively, is continuous in displacement, angle, moment and shear force. Node *D* is a loose end with no moment or shear force. Node *E* and *H* have an additional point mass, inertia and stiffness due to the gearbox or rotor (support), respectively.

Using the BC's described in table 3.1 in equation 2.6 and solving for the resonance frequencies  $\omega_n$ , results in the following (manually scaled) modeshapes, shown in figure 3.3. Here, the rotor is the left (magenta) mass and the gearbox the right one. The tower is shown right as **red** square mark with grey line. The first three Eigenfrequencies, shown at the *y*-axis, are within the speed range of the DC driving motor of the test bench.

The second and third mode are highly sensitive on the gearbox spring stiffness  $k_{GB}$ , as can be seen by the amplitude in *z*-direction of the gearbox. Therefore, also a part of the High Speed Shaft (HSS) may need to be included in the model, since its mass and coupling stiffness influence the gearbox motion. The structural model assumes only gearbox movement, while its torsion rotation is fixed. This may not be the case for the test bench, causing inaccuracies for the load prediction.

In this research, the analytic model is used to determine the dimensions of the test bench during the design phase, get insight in its dynamic behaviour and verify results of other methods. It is not used to describe the relation between displacements and loads, because modeshape scaling of multiple linked beams is too complicated. Therefore the FEM approach is applied to the test bench in the next section.

Appendix B.2 gives a short documentation how this analytic approach is defined in a Matlab file.

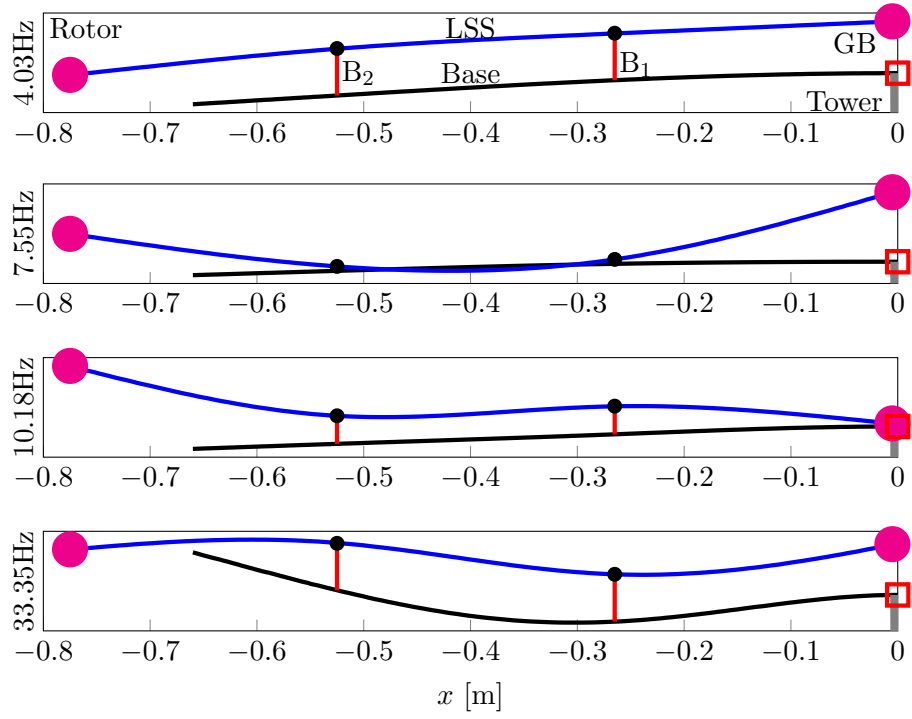


Figure 3.3: Schematic overview analytic modeshapes with Eigenfrequencies  $\omega$ ,  $XZ$  plane.

### 3.2 FEM - Spacar

Using FEM program Spacar [30] (extended version) modeshapes are determined, as can be seen in figure 3.4. The same grid as with the analytic approach is used. Bending and torsion in 3D is considered. The rotor is mounted on the (blue) LSS end as magenta disc. The gearbox is modelled as beam element, instead of a point-mass in the analytic model. The right edge of the magenta gearbox is also supported by a grey spring  $k_{GB}$ , allowing rotation of the gearbox (shaft torsion). The bearings (red blocks) are modelled as rigid beams. As it can be seen, the

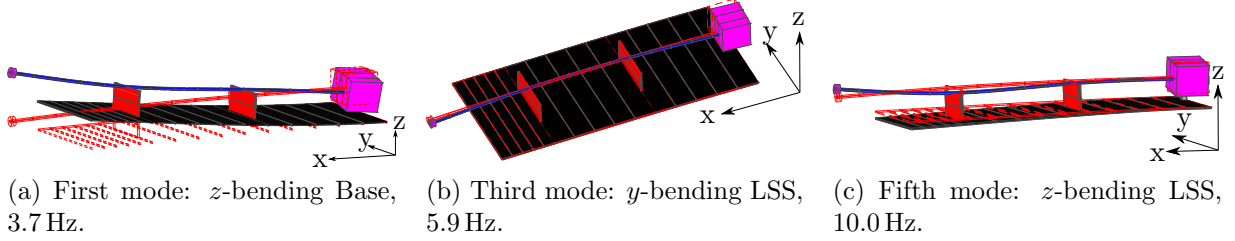


Figure 3.4: Schematic overview three Spacar modeshapes.

first (figure 3.4a) and fifth (figure 3.4c) mode correspond to the analytic solutions of figure 3.3. The second mode (not shown) is shaft torsion in combination with a rotation of the gearbox at 5.8 Hz. The third (figure 3.4b) and fourth (not shown) modes are LSS bending in  $y$ -direction, which were not modelled analytically. Also these are dominated by the radial gearbox spring stiffness  $k_{GB}$  in  $y$ -direction. The fifth mode is the second bending mode in  $z$ -direction of the LSS.

The shaft bending in  $y$ -direction is almost similar to the one in  $z$ -direction, but depends on the gearbox side ways spring stiffness  $k_{GB,y}$ . Therefore, the model may be simplified by disregarding the  $y$ -bending in 3D. Appendix B.3 gives a short documentation of the input file for Spacar.

However, a complete understanding of the node numbering inside Spacar matrices is required in order to use Spacar to process acceleration data. This is not possible since numbering is done internally. Besides this, gearbox torsion in combination with gears can not be added to the program. Another disadvantage is the limitation to the amount of beams of the program. Therefore, Spacar is only used to verify the Eigenfrequencies and modeshapes of the manual programmed FEM approach.

### 3.3 FEM - Defined manually

In this section the description of the manual FEM applied to the test bench is described. The coordinate system and linking of the beam elements can be put to a desired set for data processing by manually programming the model. Also extra constraints like the gear ratio can be added by using the Lagrange multiplier theorem. Because the FEM model is programmed manually, it is relatively simple and fast. This section explains the definition of the model elements, boundary conditions, linking between different elements and damping of the FEM model of the test bench.

#### 3.3.1 Elements

The test bench geometry is simplified to a beam structure with different element (colours) per different cross section, as shown in figure 3.5; it is similar to the real test bench shown in figure A.1. As can be seen by the element colours, the FEM model consists of different beam elements. Each one is described as follows:

1. **Base** (black line): A beam element with bending in  $z$ -direction, fixed at the tower (grey rectangle), coupled to the LSS and generator (GEN) by bearing  $B_2$ ,  $B_1$ ,  $B_3$   $B_4$ , shown as red lines with a black dot. These are modelled as spring, described in detail in section 3.3.3. The numbering is due to the model definition of the FEM elements. Viscous friction can be neglected [37]. Two accelerometers  $ac$  are located below the main bearings  $B_2$  and  $B_1$ , shown as orange squares. The Base is clamped to the tower. The right part of the base, between the tower and generator is stiffened to give it higher resonance frequencies.
2. **LSS** (blue line): A shaft beam element with bending in  $z$ -direction and torsion around the



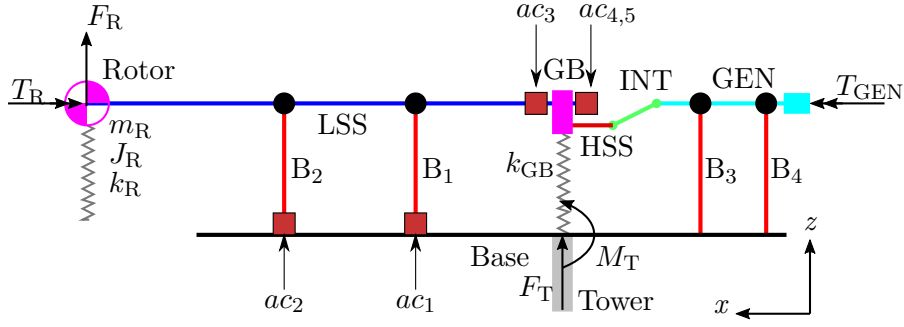


Figure 3.5: Schematic overview of manual FEM structural model with external loads.

$x$ -axis ( $\psi$ ). The rotor is added as point inertia and is supported with stiffness  $k_R$ . The right part overlaps with the gearbox (GB). Two accelerometers are added to the LSS beam element at nodes near the GB, shown as orange squares.

3. **GB** (magenta line): A beam element bending in  $z$ -direction, parallel to the  $y$ -axis. Figure 3.6 shows an enlarged view with the gearbox in magenta. The gearbox geometry of the test bench is simplified to a simple beam with corresponding mass and inertia. One accelerometer is added to the gearbox beam element. The gearbox spring ( $k_{GB}$ ) is added as translation and rotation stiffness. These stiffness is determined experimentally. As can be seen below, the GB is only linked to the LSS and HSS by two 'bearing nodes' (where the GB beam crosses the LSS and HSS shafts), instead of the four bearings in the real test bench. This is because of simplicity reasons. The linking (or merging) to the LSS and HSS by Lagrange multipliers is explained in section 2.2.2.
4. **HSS** (red line): A torsion beam element with bending in  $z$ -direction and torsion around the  $x$ -axis ( $\psi$ ) and is coupled to an intermediate shaft (INT) by a membrane coupling. The coupling is shown as sphere mark.
5. **INT** (green line): A torsion beam element with bending in  $z$ -direction and torsion around the  $x$ -axis ( $\psi$ ) and is coupled to the generator (GEN) by a membrane coupling.
6. **GEN** (cyan line): A torsion beam element with bending in  $z$ -direction and torsion around the  $x$ -axis ( $\psi$ ). The mass and inertia of both the solid coupling to the DC motor and generator are included in the beam by a thicker shaft radius.

Each beam element has a mass and stiffness matrix  $\mathbf{M}$  and  $\mathbf{K}$ . The accelerometer mass and inertia is taken into account. The linking using bearings, couplings or Lagrange multipliers will be described in the next sections.

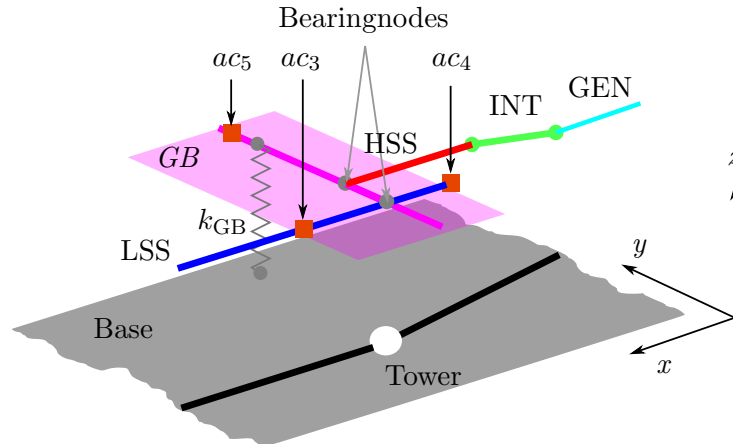


Figure 3.6: Schematic overview gearbox manual FEM structural model, enlarged 3D view.

### 3.3.2 Boundary conditions

The connections to the ground or outside world have to be defined. The rotor angle  $\psi_R$  is assumed driven at constant angular speed  $\Omega$ , for the model this implies it does not have a speed

variation. The following external unknown loads are derived from figure 3.5:

1. Rotor force  $F_R$  in  $z$ -direction, due to the constant angular speed.
2. Rotor torque  $T_R$  in  $\psi$ -direction, due to gravity acting on the unbalance arm.
3. Generator torque  $T_{\text{GEN}}$ , because of electric resistance.
4. Clamping force  $F_T$  at the tower fixation. The displacement  $z$  is zero at the tower.
5. Clamping moment  $M_T$  at the tower fixation. The inclination angle  $\theta$  is zero at the tower.

### 3.3.3 Link LSS to Base

The main and generator bearings link the base displacement to the LSS and HSS, respectively. Since the bearings have a finite axial stiffness, they can be modelled as tension-compression spring elements. An additional benefit is that the load in this spring elements can be easily evaluated for a given displacement profile. This section applies this principle to the main bearings, but also holds for the generator bearings.

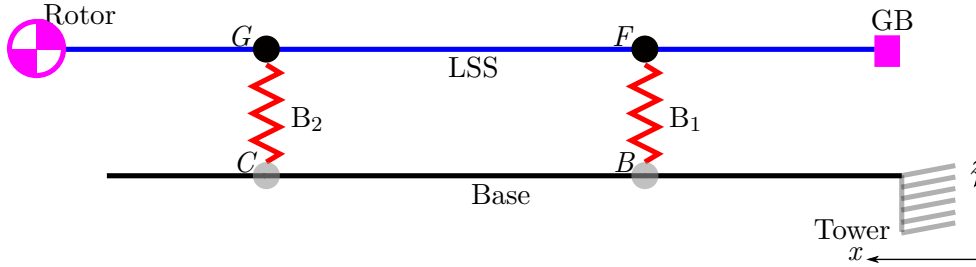


Figure 3.7: Schematic overview linking LSS to the Base by linear bearing spring elements.

Figure 3.7 shows a schematic overview of the part of the base frame, the main bearings, the LSS and GB, with illustrative node numbering in capital letters  $B$ ,  $C$ ,  $F$  and  $G$ . The stiffness matrix  $\mathbf{K}$  of the Base and LSS combined look as shown in equation 3.1. The same holds for the mass matrix  $\mathbf{M}$ , shown in equation 3.2.

$$\mathbf{K} = \begin{bmatrix} [\mathbf{K}_{\text{Base}}] & \mathbf{0} \\ \mathbf{0} & [\mathbf{K}_{\text{LSS}}] \end{bmatrix} \quad (3.1)$$

$$\mathbf{M} = \begin{bmatrix} [\mathbf{M}_{\text{Base}}] & \mathbf{0} \\ \mathbf{0} & [\mathbf{M}_{\text{LSS}}] \end{bmatrix} \quad (3.2)$$

The bearing stiffness matrix  $\mathbf{K}_b$  with linear (radial) bearing stiffness  $k_b$  is given by:

$$\mathbf{K}_b = k_b \begin{bmatrix} 1 & -1 \\ -1 & 1 \end{bmatrix} \quad (3.3)$$

The lumped bearing mass matrix  $\mathbf{M}_b$  is given by bearing mass  $m_b$ , distributed equally over the two nodes:

$$\mathbf{M}_b = \frac{1}{2} m_b \begin{bmatrix} 1 & 0 \\ 0 & 1 \end{bmatrix} \quad (3.4)$$

The bearings only constrain  $z$ -displacement between nodes  $C$  and  $G$  and as well as between node  $B$  and  $F$ . The bearing stiffness and mass matrices are added to the total matrices of equations 3.1 and 3.2, for example for bearing  $B_2$  on nodes  $C$  and  $G$ :

$$\mathbf{K}([C_z, G_z], [C_z, G_z]) = \mathbf{K}([C_z, G_z], [C_z, G_z]) + \mathbf{K}_b \quad (3.5)$$

$$\mathbf{M}([C_z, G_z], [C_z, G_z]) = \mathbf{M}([C_z, G_z], [C_z, G_z]) + \mathbf{M}_b \quad (3.6)$$

This is done for all four bearings  $B_1$ ,  $B_2$ ,  $B_3$  and  $B_4$  of the test bench. It also applies to the membrane couplings, but these have stiffness in three directions ( $z$ ,  $\theta$  and  $\psi$ ), resulting in 6x6 matrices.

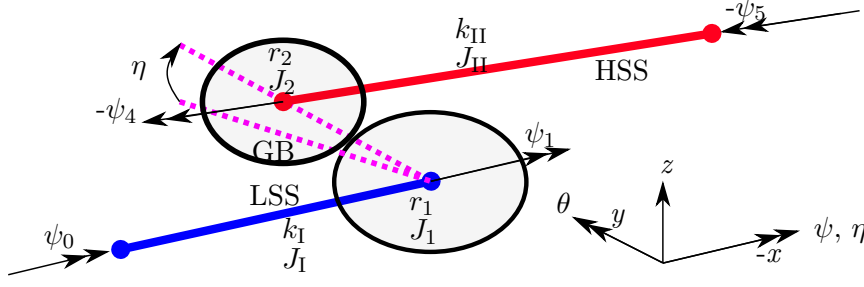


Figure 3.8: Schematic overview of a one stage gearbox with DoFs and applied torques.

### 3.3.4 Link between GB, LSS and HSS

The Lagrange multiplier theorem will be applied to the gearbox, since at the gearbox, the LSS, HSS and the gears are physical linked together by bending and rotation. The LSS, HSS and GB elements are shown schematically in figure 3.8 in respectively blue, red and magenta colours. The gearbox has a degree of freedom (DoF) around the  $x$ -axis:  $\eta$ . Where the angular displacement of a node is shown by  $\psi$ , the torsional shaft stiffness  $k_I$  and  $k_{II}$  is given by the third and sixth row or column, respectively, in equation 2.28, the rotational mass inertia by  $J$  and the gear radius by  $r$ . The node numbering 1 to 5 is illustrative.

This section first compares the gear teeth stiffness with LSS torsional stiffness. Second it describes the link the LSS, HSS and GB rotations by the torsional stiffness matrices. Thirdly the bending of the LSS and HSS is linked. Both links are needed to fully describe the physical connections of test bench in the structural FEM modal.

### Stiffness comparison between gear teeth and LSS

The stiffness of the teeth is considered in figure 3.9, with a schematic overview of the two gears with two teeth. The right (blue dot) gear is mounted on the LSS, the left (red dot) gear is mounted on the HSS. Both rotate opposite to each other, since it is a one-stage gearbox. With

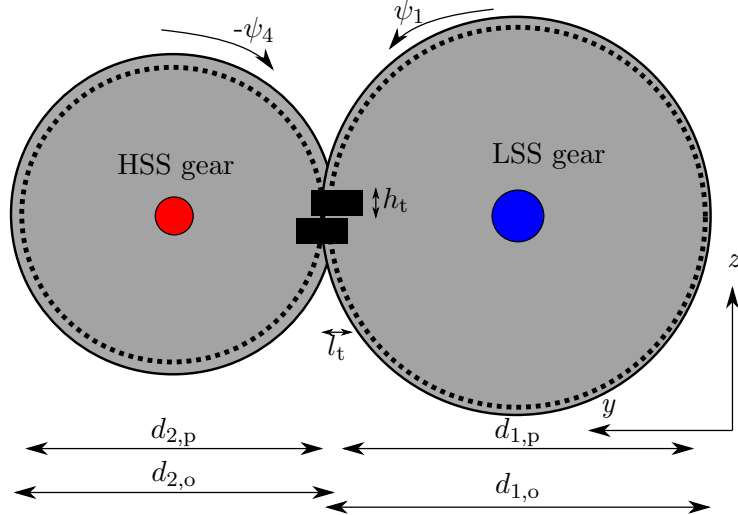


Figure 3.9: Schematic YZ-overview of gears with two teeth.

parameters described in table 3.2 from [38]. Where teeth length  $l_t$  is assumed to be half of the difference between the outer and pitch radius  $d_o$  and  $d_p$ . The teeth height  $h_t$  is assumed by:

$$h_t = \frac{\pi d_p}{2n} \quad (3.7)$$

With  $n$  the number of teeth. The rotation stiffness of one gear teeth  $k_g$  using beam bending theory is:

$$k_g = \frac{T}{\psi} = \frac{3EI r^2}{l_t^3} \quad (3.8)$$

Table 3.2: Characteristic quantities gears.

Parameter	Quantity	Value	Unit
$d_{1,o}$	Outer diameter gear 1	38	mm
$d_{2,o}$	Inner diameter gear 2	17	mm
$d_{1,p}$	Pitch diameter gear 1	36	mm
$d_{2,p}$	Pitch diameter gear 2	15	mm
$h_t$	Teeth height	1.6	mm
$l_t$	Teeth length	1.0	mm
$n_1$	No teeth gear 1	36	-
$n_2$	No teeth gear 2	15	-
$w_t$	Gear width	6.0	mm

Here  $T$  is the torque on the shaft,  $\psi$  the shaft rotation,  $E$  is the E-modulus of polyoxymethylene (POM),  $r$  the pitch radius and  $I$  the area inertia of the teeth cross section ( $w_t \times l_t$ ) and is the gear disc assumed rigid. The total stiffness  $k_{gears}$  of both gears is combined:

$$k_{gears} = \left( \frac{1}{k_{g1}} + \frac{1}{k_{g2}} \right)^{-1} = 912.8 \quad [\text{Nm/rad}] \quad (3.9)$$

The LSS torsion stiffness is given by:

$$k_{LSS,\psi} = \frac{T}{\phi} = \frac{GI_{xy}}{l_s} = 12.7 \quad [\text{Nm/rad}] \quad (3.10)$$

With shear modulus  $G$  is 70 GPa for steel, shaft length  $l_s$  is 700 mm and a shaft diameter of 6.0 mm. By comparing the results of equations 3.9 and 3.10, it can be seen that for the test bench the gear teeth stiffness  $k_{gears}$  is about a factor seventy higher compared to the shaft torsion stiffness  $k_{LSS,\psi}$ . Therefore the gear teeth are assumed rigid.

### Torsion linking of the LSS, HSS and GB rotation

As the gear teeth are assumed rigid compared to the LSS torsion stiffness, the following constraint equation between the LSS, HSS and gearbox rotation  $\eta$  is derived from figures 3.8 and 3.9:

$$\Phi = -N\psi_1 - \psi_4 + \eta = 0 \quad (3.11)$$

With the gear ratio  $N$  is defined as  $r_1/r_2$  and where shaft rotation  $\psi_4$  is dependent on shaft rotation  $\psi_1$  and gearbox rotation  $\eta$ . This constraint equation can be used to link the LSS and HSS mass and stiffness matrices  $\mathbf{K}$  and  $\mathbf{M}$ , as was shown in figure 3.8. The LSS and HSS shaft elements have both just common  $\mathbf{K}$  and  $\mathbf{M}$  matrices for torsion, with  $\mathbf{q}$  defined as:

$$\mathbf{q} = [\psi_0, \psi_1, \eta, \psi_4, \psi_5]^T \quad (3.12)$$

$$\mathbf{K} = \begin{bmatrix} k_I & -k_I & 0 & 0 & 0 \\ -k_I & k_I & 0 & 0 & 0 \\ 0 & 0 & 0 & 0 & 0 \\ 0 & 0 & 0 & k_{II} & -k_{II} \\ 0 & 0 & 0 & -k_{II} & k_{II} \end{bmatrix} \quad (3.13)$$

Lumped mass matrix  $\mathbf{M}$ , but with added point inertia of the gears  $J_1$  and  $J_2$  at the gear nodes, is given by:

$$\mathbf{M} = \begin{bmatrix} \frac{1}{2}J_I & 0 & 0 & 0 & 0 \\ 0 & \frac{1}{2}J_I + J_1 & 0 & 0 & 0 \\ 0 & 0 & 0 & 0 & 0 \\ 0 & 0 & 0 & \frac{1}{2}J_{II} + J_2 & 0 \\ 0 & 0 & 0 & 0 & \frac{1}{2}J_{II} \end{bmatrix} \quad (3.14)$$

As can be seen by the absence of off-diagonal terms between the second, third and fourth rows or columns, respectively, there is no linking between the nodes  $\psi_1$  and  $\psi_4$ . Applying the matrix reduction to the  $\mathbf{K}$  and  $\mathbf{M}$  matrices by using the Lagrange multiplier of equation 2.39 results in the following reduced  $\hat{\mathbf{K}}$  and  $\hat{\mathbf{M}}$  matrices, with independent variables  $\mathbf{q}_i$ , chosen as  $[\psi_0, \psi_1, \eta, \psi_5]^T$  and dependent variable  $q_d$  is  $[\psi_4]$ :

$$\hat{\mathbf{K}} = \begin{bmatrix} k_I & -k_I & 0 & 0 \\ -k_I & k_I + k_{II}N^2 & -k_{II}N & k_{II}N \\ 0 & -k_{II}N & k_{II} & -k_{II} \\ 0 & k_{II}N & -k_{II} & k_{II} \end{bmatrix} \quad (3.15)$$

$$\hat{\mathbf{M}} = \begin{bmatrix} \frac{1}{2}J_I & 0 & 0 & 0 \\ 0 & \frac{1}{2}J_I + J_1 + N^2(J_2 + \frac{1}{2}J_{II}) & -N(J_2 + \frac{1}{2}J_{II}) & 0 \\ 0 & -N(J_2 + \frac{1}{2}J_{II}) & J_2 + \frac{1}{2}J_{II} & 0 \\ 0 & 0 & 0 & \frac{1}{2}J_{II} \end{bmatrix} \quad (3.16)$$

Shaft rotation  $\psi_4$  is replaced by gearbox rotation  $\eta$ , keeping the size of the original matrices of the LSS and HSS the same, which is convenient for programming. Wu et al. [39] determined similar mass and stiffness matrices for adding gearbox ratios to shaft elements, but with a fixed gearbox housing rotation  $\eta$ . This is an extra validation of the used linking method. As can be seen by the off-diagonal terms, the rotation coordinates are now linked together.

### Bending linking of the LSS, HSS and GB

The gearbox rotation can be added to the LSS and HSS rotations and displacements including the gear ratio. The gearbox housing is modelled also as a rigid beam with mass, but perpendicular (radial) to the shafts and parallel to the  $y$ -axis. This is visualized in figure 3.10, where all DoF per node are shown for the LSS, GB and HSS beams. Shaft rotation  $\psi$  is due to torsion, rotation  $\phi$  is due to a bending moment. Shaft rotation  $\psi_4$  is replaced by  $\eta$  as was described previously. The node numbering 1 to 5 is illustrative. The figure has the same orientation and colouring as figure 3.6. Four constraint equations  $\Phi$  are applied to link the different elements (colours) of figure

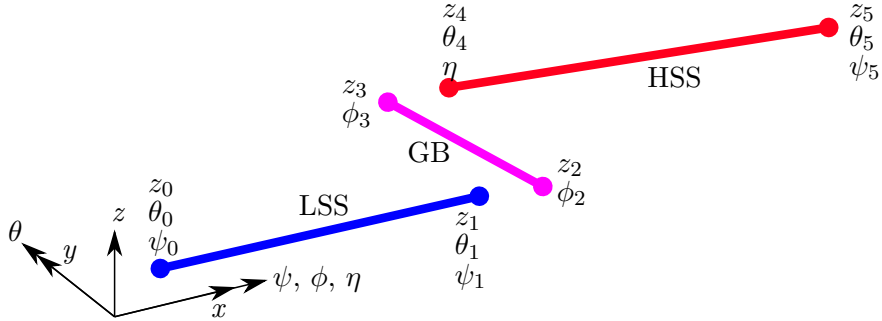


Figure 3.10: Schematic overview LSS, GB and HSS beams with DoF per node, not linked.

3.10 to each other. These four constraints are needed to constrain the degrees of freedom of the gearbox. Gearbox angle  $\eta$  is dependent of shaft rotation  $\psi_3$  of the gearbox element, resulting in the following constraint equation with merged angles:

$$\Phi_1 = -\eta + \psi_3 = 0 \quad (3.17)$$

The gearbox beam element is also coupled to the LSS and HSS by displacements. This results in the following constraint equations:

$$\Phi_2 = z_1 - z_2 = 0 \quad (3.18)$$

$$\Phi_3 = -z_3 + z_4 = 0 \quad (3.19)$$

Also, angle  $\theta$  is continuous through the gearbox. This implies:

$$\Phi_4 = \theta_1 - \theta_4 = 0 \quad (3.20)$$

Combining these four constraint equations, choosing dependent coordinates  $\mathbf{q}_d$  as  $[\eta, z_2, z_3, \theta_4]^T$  and applying these to the total  $\mathbf{K}$  and  $\mathbf{M}$  matrices of the system results in reduced matrices  $\hat{\mathbf{K}}$  and  $\hat{\mathbf{M}}$ , which are used to determine the modeshapes of the structural model. The next chapter will describe how the defined structural model can be manipulated to process the acceleration data.

## 4 Data processing

The structural model was defined in section 3.3. Before it can be used, the model matrices need to be manipulated according to known and unknown coordinate values in order to use them in combination with the accelerometer data. The accelerometers can have some offset to a maximum of 15% or measure unnecessary vibrations, such as higher harmonics. Higher harmonics are not modelled in the structural model. Therefore, the measurement data needs to be pre-processed before it can be used as input for the structural model. This can be done by applying a detrending method to the data and using filter techniques. After filtering the data can be used as input for the model to determine (internal) loads.

### 4.1 Acceleration measurements filtering

Accelerometers have a voltage as output with a given relation between the voltage and acceleration. For the used accelerometers, this relation is assumed to be constant and determined by a calibration done once in the past. However, in experiments a small offset was observed, making measurements less accurate. Since the accelerations are assumed to be harmonic, as stated in section 2.21, the offset should be zero. This is done by detrending the data, where the mean value of the data is removed [40].

Besides the unwanted offset, the data also contains higher harmonics and noise due to external vibrations. A band pass filter can be used to remove frequencies below and above the harmonic frequencies, which are multiples of the rotational speed  $\Omega$ . Another disturbance at a multiple of the gearbox ratio is the HSS rotational speed  $\Omega_{HSS}$ . The filter can be described in the Laplace domain ( $s$ ) by [41]:

$$BP(s) = \frac{\Delta\Omega s}{s^2 + \Delta\Omega s + \Omega^2} \quad (4.1)$$

The frequency difference  $\Delta\Omega$  is the peak width to pass through and is chosen to be 1.0 Hz based on iterations. Frequencies below this band width at frequency  $\Omega$  are suppressed.

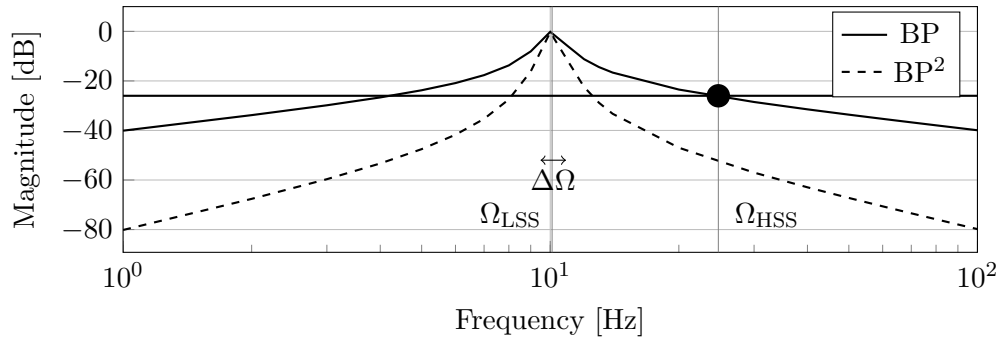


Figure 4.1: Bode diagram of bandpass filters for 604 RPM rotational rotor speed.

Figure 4.1 shows the frequency spectrum with a second-order and a quadratic bandpass filter at  $\Omega_{LSS}$ . The quadratic filter ( $BP^2$ ) is needed in stead of the second order bandpass filter  $BP$ , because the second-order filter has a too small amplification factor of about  $-25$  dB at the other peak, as can be seen in figure 4.1 at the black mark. An amplification of  $-25$  dB does not suppress the other peak sufficiently. The slope of the quadratic filter is  $-40$  dB per decade, while the second order is only  $-20$  dB. The phase plot is not shown, because the phase-shift is compensated automatically by Matlab and neglected during data processing [42].

### 4.2 From acceleration measurements to loads

Figure 4.2 shows a flow diagram of the load prediction algorithm based on acceleration measurements. The structural model was defined in section 3.3, but the mass and stiffness matrices need to be manipulated and shuffled according to knowns and unknowns to determine loads from

acceleration measurements. This is described in this section. First the assumptions and needed inputs are stated. Second the manipulation of the matrices is explained.

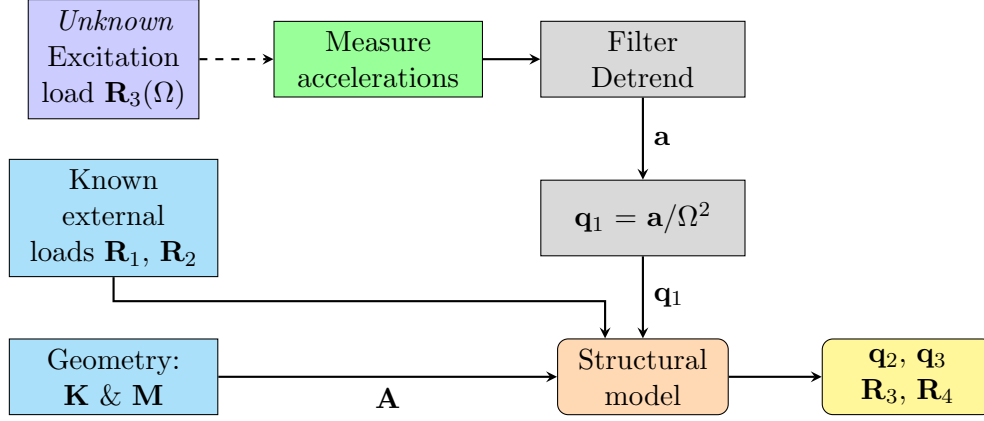


Figure 4.2: Flow diagram algorithm to predict forces with acceleration measurements as input.

#### 4.2.1 Structural model inputs

The first described inputs are the accelerometers. The test bench drive train rotates an un-balanced rotor with rotational speed  $\Omega$ , resulting in an harmonic excitation load  $\mathbf{R}_3$ . This is causing harmonic vibrations. These harmonic vibrations are measured with accelerometers at certain nodes as was described in section 3.3.1. The acceleration measurements are filtered and detrended, as described in section 4.1. Because of the harmonic profile,  $\mathbf{q}_1$  due to the acceleration at a node can be determined from:

$$\mathbf{q}_1 = -\frac{\mathbf{a}}{\Omega^2} \quad (4.2)$$

Where acceleration  $\mathbf{a}$  is filtered with a bandpass filter at frequency  $\Omega$ .

The second inputs are the known external loads  $\mathbf{R}_1$  and  $\mathbf{R}_2$ . These loads are zero because only the dynamic external loads on nodes are considered; the static force due to gravity is not taken into account. For example, see figure 3.5 for the external loads. In this figure, all nodes of the LSS except for the rotor node have zero external force.

The third inputs are the  $\mathbf{K}$  and  $\mathbf{M}$  matrices are given by the geometry of the test bench. The 'dynamic stiffness matrix'  $\mathbf{A}$  is described from equation 2.25 by:

$$\mathbf{A} = [-\Omega^2\mathbf{M} + i\Omega\mathbf{C} + \mathbf{K}] \quad (4.3)$$

#### 4.2.2 Manipulation of dynamic stiffness matrix $\mathbf{A}$

A manipulation of matrix  $\mathbf{A}$  is proposed by linear algebra according to knowns and unknowns of variable  $\mathbf{q}$  and loads  $\mathbf{R}$ :

$$\begin{bmatrix} \mathbf{A}_{11} & \mathbf{A}_{12} & \cdot & \cdot \\ \mathbf{A}_{21} & \cdot & \cdot & \cdot \\ \cdot & \cdot & \cdot & \cdot \\ \cdot & \cdot & \cdot & \mathbf{A}_{44} \end{bmatrix} \cdot \begin{bmatrix} \mathbf{q}_1 \\ \mathbf{q}_2 \\ \mathbf{q}_3 \\ \mathbf{q}_4 \end{bmatrix} = \begin{bmatrix} \mathbf{R}_1 \\ \mathbf{R}_2 \\ \mathbf{R}_3 \\ \mathbf{R}_4 \end{bmatrix} \quad (4.4)$$

As can be seen in equation 4.4, there are four 'row sections' 1 to 4. Each section consists of multiple rows. Each section has a different meaning in the sense of known and unknown values, as can be seen in table 4.1. Unknown values ( $uv$ ) need to be determined using the structural model.



Table 4.1: Explanation row sections system of equations.

Row sec.	$\mathbf{q}$	$\mathbf{R}$	Remark
1	measured	0	Nodes with accelerometers
2	$uv$	0	Nodes without ex. load
3	$uv$	$uv$	Nodes with ex. load
4	0	$uv$	Clamped nodes

Note, the sequence of the rows can be chosen arbitrarily. As can be seen, row section one should have the same or larger size than row section three in order to solve this system of equations.

Unknown variables  $\mathbf{q}_2$  and  $\mathbf{q}_3$  can be determined from the known loads  $\mathbf{R}_1$  and  $\mathbf{R}_2$  and variables  $\mathbf{q}_1$  by an inverse FEM approach:

$$\begin{bmatrix} \mathbf{q}_2 \\ \mathbf{q}_3 \end{bmatrix} = \begin{bmatrix} \mathbf{A}_{12} & \mathbf{A}_{13} \\ \mathbf{A}_{22} & \mathbf{A}_{23} \end{bmatrix}^{-1} \cdot \left( \begin{bmatrix} \mathbf{R}_1 \\ \mathbf{R}_2 \end{bmatrix} - \begin{bmatrix} \mathbf{A}_{11} \\ \mathbf{A}_{21} \end{bmatrix} \mathbf{q}_1 \right) \quad (4.5)$$

Variables  $\mathbf{q}_2$  and  $\mathbf{q}_3$  contain complex numbers, because matrix  $\mathbf{A}$  contains complex numbers due to the damping matrix. Since the prediction is only about the magnitude of the excitation only the real part is taken into account. The inverse is not necessarily square, so in most cases the pseudo-inverse is used.

With all variables of  $\mathbf{q}$  determined, the external loads  $\mathbf{R}_3$  and  $\mathbf{R}_4$  can be determined using equation 4.4, again considering only the real part of the solution:

$$\begin{bmatrix} \mathbf{R}_3 \\ \mathbf{R}_4 \end{bmatrix} = \begin{bmatrix} \mathbf{A}_{31} & \mathbf{A}_{32} & \mathbf{A}_{33} \\ \mathbf{A}_{41} & \mathbf{A}_{42} & \mathbf{A}_{43} \end{bmatrix} \cdot \begin{bmatrix} \mathbf{q}_1 \\ \mathbf{q}_2 \\ \mathbf{q}_3 \end{bmatrix} \quad (4.6)$$

#### 4.2.3 Structural model output

Using the complete set of  $\mathbf{q}$  and the mass and stiffness matrices  $\mathbf{M}_e$  and  $\mathbf{K}_e$  for each element, all dynamic internal loads can be determined. For example the bearing loads with element matrices described in equation 3.1. Also the rotor force  $F_{R,z}$  can be predicted. This prediction can be compared with the theoretical value using equation 1.2. The rotor origin acceleration has to be taken into account.

### 4.3 From theoretical rotor force to accelerations

The proposed algorithm of section 4.2 is partly modified or reverted to predict accelerations based on the rotor force described in equation 1.2. This is needed as validation of the model and to quantify the prediction error. Figure 4.3 shows a flow diagram of the used algorithm and is explained in this section.

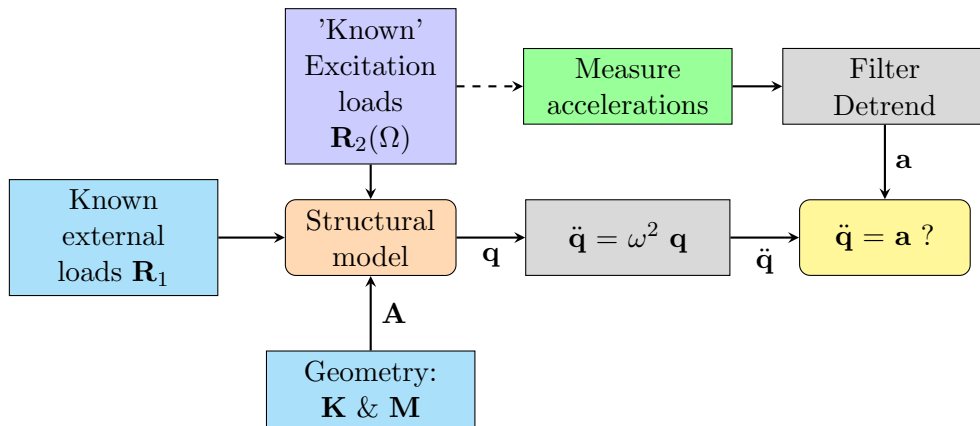


Figure 4.3: Algorithm assumed forces to predict accelerations.

#### 4.3.1 Structural model inputs

The first inputs are the known external loads  $\mathbf{R}_1$ . These loads are zero because only the dynamic external loads on nodes are considered; static gravity load is not taken into account. For example,

see figure 3.5. In this figure, all nodes of the LSS except for the rotor node have zero external force. The loads by the rotor  $\mathbf{R}_2$  are derived from the free body diagram shown in figure 1.7. The acceleration of the rotor origin  $\ddot{z}$  is neglected in this case, because it is also unknown. This has as implication that the prediction only holds for frequencies where the acceleration of the origin is relatively small compared to the centrifugal term of the rotor acceleration. Other inputs for the model are the stiffness and mass matrices  $\mathbf{K}$  and  $\mathbf{M}$ . These are given by the geometry of the test bench. The 'dynamic stiffness matrix'  $\mathbf{A}$  was already described by equation 4.3.

#### 4.3.2 Manipulation of dynamic stiffness matrix $\mathbf{A}$

Matrix  $\mathbf{A}$  is shuffled according to known and unknown ( $uv$ ) parts of coordinates  $\mathbf{q}$  and loads  $\mathbf{R}$ :

$$\begin{bmatrix} \mathbf{A}_{11} & \mathbf{A}_{12} & \mathbf{A}_{13} \\ \mathbf{A}_{22} & . & . \\ \mathbf{A}_{32} & . & . \end{bmatrix} \cdot \begin{bmatrix} \mathbf{q}_1 \\ \mathbf{q}_2 \\ \mathbf{q}_3 \end{bmatrix} = \begin{bmatrix} \mathbf{R}_1 \\ \mathbf{R}_2 \\ \mathbf{R}_3 \end{bmatrix} \quad (4.7)$$

As can be seen, there are three 'row sections'. Each can consist of multiple rows. Each section has a different meaning in the sense of known and unknown values:

Table 4.2: Explanation row sections system of equations.

Row sec.	$\mathbf{q}$	$\mathbf{R}$	Remark
1	$uv$	0	Nodes without ex. load
2	$uv$	Rotor load	Assumed load
3	0	$uv$	Clamped nodes

Loads  $\mathbf{R}_1$  and  $\mathbf{R}_2$  are used as input in the structural model to determine the unknown variables  $\mathbf{q}_1$  and  $\mathbf{q}_2$  using an inverse FEM approach:

$$\begin{bmatrix} \mathbf{q}_1 \\ \mathbf{q}_2 \end{bmatrix} = \begin{bmatrix} \mathbf{A}_{12} & \mathbf{A}_{13} \\ \mathbf{A}_{22} & \mathbf{A}_{23} \end{bmatrix}^{-1} \cdot \begin{bmatrix} \mathbf{R}_1 \\ \mathbf{R}_2 \end{bmatrix} \quad (4.8)$$

Because this inverse is not necessarily square, in most cases the pseudo-inverse is used.

#### 4.3.3 Structural model output

Matrix  $\mathbf{A}$  contains complex numbers due to damping. Only the real part of  $\mathbf{q}_1$  and  $\mathbf{q}_2$  is taken into account. Multiplying  $\mathbf{q}$  with  $-\Omega^2$  by equation 2.3 results in predicted accelerations. These can be compared with the filtered acceleration measurements.

## 5 Validation results and discussion

Validation of the model is needed to show and quantify its quality and accuracy. A maximum error of 2.15% is allowed in this research, as was based on the  $L_{10}$  norm in section 1.4. The quality of the prediction is important, because a small error in load prediction can make a big difference in the remaining lifetime prediction. First a rough validation of the sensors to trust the externally done calibration is provided. Second the modeshapes of the structural model and the test bench are compared. These modeshapes describe the response of the system to a certain load, as described in the analytic approach of section 2.1. At last, a reversed model is used with assumed rotor loads as input to predict accelerations at measurement nodes, which can be compared to acceleration measurements at the test bench. This comparison can be used to determine the quality of the model.

### 5.1 Sensor validation

The 3D acceleration sensors were calibrated externally in the past. A rough validation with a yard stick is done to verify the motion amplitudes of the sensors. Besides the amplitude also the rotor speed  $\Omega$  is measured for verification, since this is related to the accelerations in the system. An external RPM meter is placed at the generator shaft of the test bench, as can be seen in figure 5.1. The generator rotates with a speed ratio  $N$  of 2.45:1 due to the gearbox.

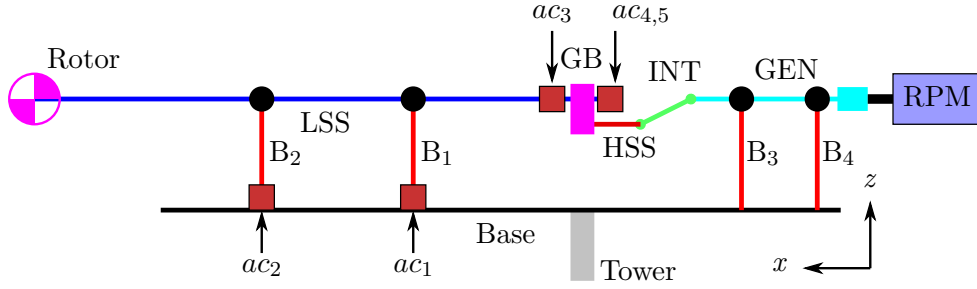


Figure 5.1: Schematic overview of the RPM meter located at the generator shaft end.

The vibrations due to the unbalanced rotor are measured by accelerometers  $ac_1$  till  $ac_5$ . The measurements are transformed from the time domain to the frequency domain by the Fourier transformation. A plot of the frequency spectrum of the five sensors is shown in figure 5.2, with a sampling frequency  $f_s$  of 20.0 kHz. The absolute value is smoothed with a moving average filter with thirty points. The frequency spectrum is cropped and scaled to the maximum peak. Some important observations are stated below:

- The left peak is the rotational speed of the rotating unbalance at the LSS rotor, marked as  $\Omega_{LSS}$ . This corresponds to the (gearbox ratio converted) value measured with the external RPM meter.
- At multiples of the LSS frequency, small peaks are observed, which are due to higher harmonics. Their amplitude decrease rapidly for higher frequencies.
- The highest peak is at 2.45 times the LSS frequency, located as  $\Omega_{HSS}$ . This is not an higher harmonic but the first harmonic of the HSS, due to the gear ratio. Not only the HSS vibrates at this frequency, but also the base (sensors  $ac_1$  and  $ac_2$ ). The magnitude of this peak is significantly higher compared to the first peak. This resonance frequency is not included in the structural model; it is an un modelled additional unknown input, for example a rotating unbalance at the HSS such as a membrane coupling.

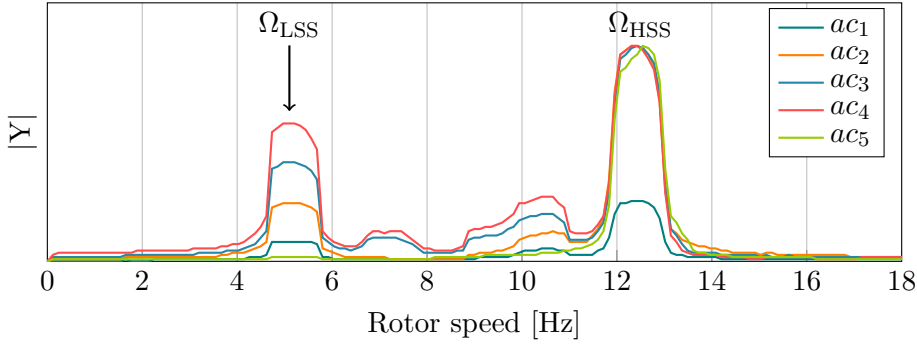


Figure 5.2: Acceleration measurements *scaled* magnitude response at 305 RPM rotor speed.

## 5.2 Modes validation

Besides the validation of the sensors, also the structural FEM model is validated. This is done by comparing the modeshapes of the test bench with the modeshapes (amplitudes) of the structural model. This is described in the following section.

### 5.2.1 Hammer Impact Test (HIT)

The response of the test bench to a certain excitation force at a specific node can be determined using an HIT. The force is applied and measured with a special impact hammer equipped with a force sensor. The response is measured with the five accelerometers  $ac_1$  till  $ac_5$ . The test bench is hit near  $ac_2$ . By using this as an hit location, the results are calibrated, since the hammer input force is measured directly with the accelerometer. This method is applied to the test bench which is shown in figure 5.3. The rotor is not driven during the HIT. It is assumed that the HIT only excites the bending modes. This assumption is allowed, since only the excitation force in  $z$ -direction of the test bench rotor is taken into account in the structural model.

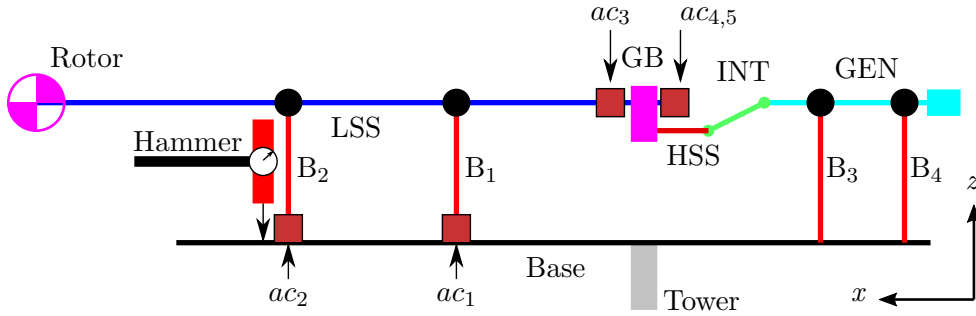


Figure 5.3: Schematic overview hammer impact test and accelerometers on structural model.

The results are visualized by dividing the output of the five accelerometers by the input force of the hammer. This is transformed to the frequency domain by the Fourier transformation (FFT), resulting in five transfer-functions between the hammer input and each accelerometer. The magnitude and phase part of the transfer-functions are shown in figure 5.4. The HIT is done twice; the results are the average of two measurement sets. The sample frequency  $f_s$  is 10.2 kHz. The frequency range is cropped to a range between 3.0 Hz and 13.0 Hz. Figure 5.4b shows the (unwrapped) phase. From this, the relative phase between the signals can be seen. This is relevant to compare with the modeshapes of the structural model. As can be seen in figure 5.4a, four resonance frequencies are present in the signal. The phase of the fifth sensor shows some noise. This can be due to the motion of the HSS part of the test bench or the gearbox motion.

### 5.2.2 Rotor speed sweep

To validate the assumption done in section 1.7.3 concerning the rotary effects on Eigenfrequencies a rotor speed sweep is done on the test bench. This is similar to the HIT, but without hammer and with rotating shafts with a varying rotor speed  $\Omega$  between 0 RPM and 600 RPM. The Fourier transform of the acceleration measurements is shown in figure 5.5. The  $y$ -axis is unscaled. The

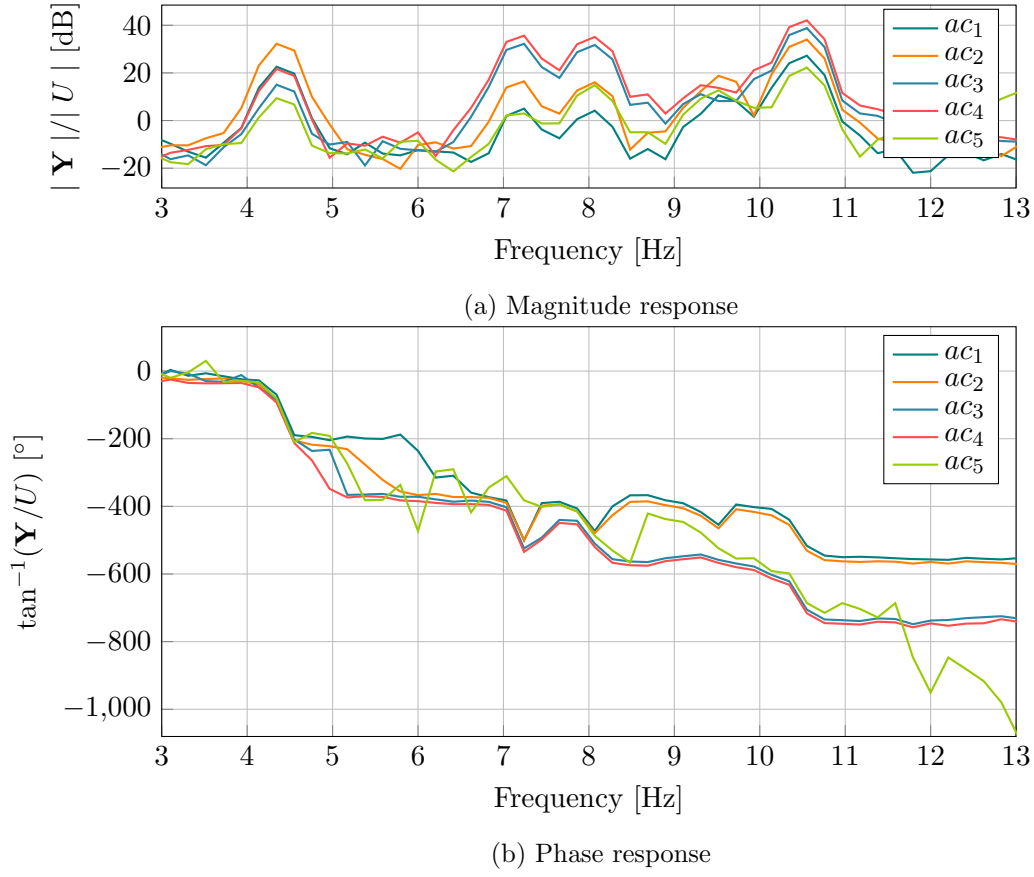


Figure 5.4: Response of accelerometers  $\mathbf{Y}$  to the impact hammer  $U$ .

sample frequency is 1.25 kHz. The absolute values of the Fourier transform are filtered using a moving average filter over thirty points. As can be seen three resonance peaks are clearly visible at 4.2 Hz, 7.1 Hz and 10.2 Hz. At 8.0 Hz also a peak is present, but this is less visible because it slightly intervenes with the second peak.

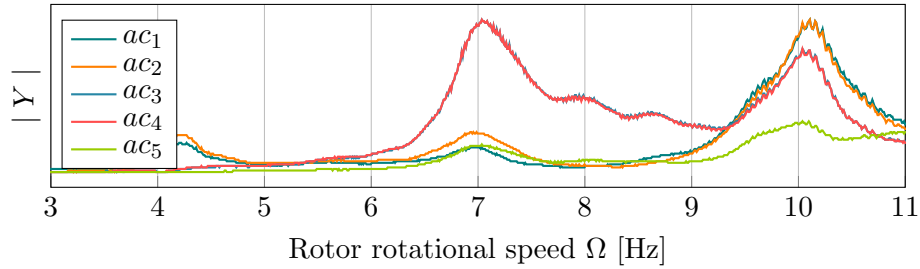


Figure 5.5: Smoothed Fourier transform of rotor speed sweep

### 5.2.3 Model modeshapes

With the system which is reduced by the Lagrange multipliers and boundary conditions, the modeshapes can be determined as shown in figure 5.6. Because torsion is relatively high frequent (about 21 Hz, lower right plot figure 5.6c), a comparison between a FEM with only bending (figure 5.6a) and with bending and shaft torsion (figures 5.6b and 5.6c) is made. For the bending-torsion model also the shafts torsion is shown at the right side. The used element colours correspond to the ones used in figure 3.5. The  $y$ -axis is unscaled, because the scaling is done manually according to a reasonable value of the gearbox rotation angle  $\eta$  around the  $x$ -axis. Some modes are mirrored due to the random scaling of the Eigenvectors. Both models use the same test bench geometry and parameters. As can be seen in figure 5.6, the difference between the two models can be found in the modeshapes where the gearbox moves. An explanation for this difference

can be the effect of extra rotational inertia and stiffness. The first torsion mode of the shafts is at 21.2 Hz. Bending of the stiffened (cyan) HSS-GEN Base part of the test bench is at 23.0 Hz.

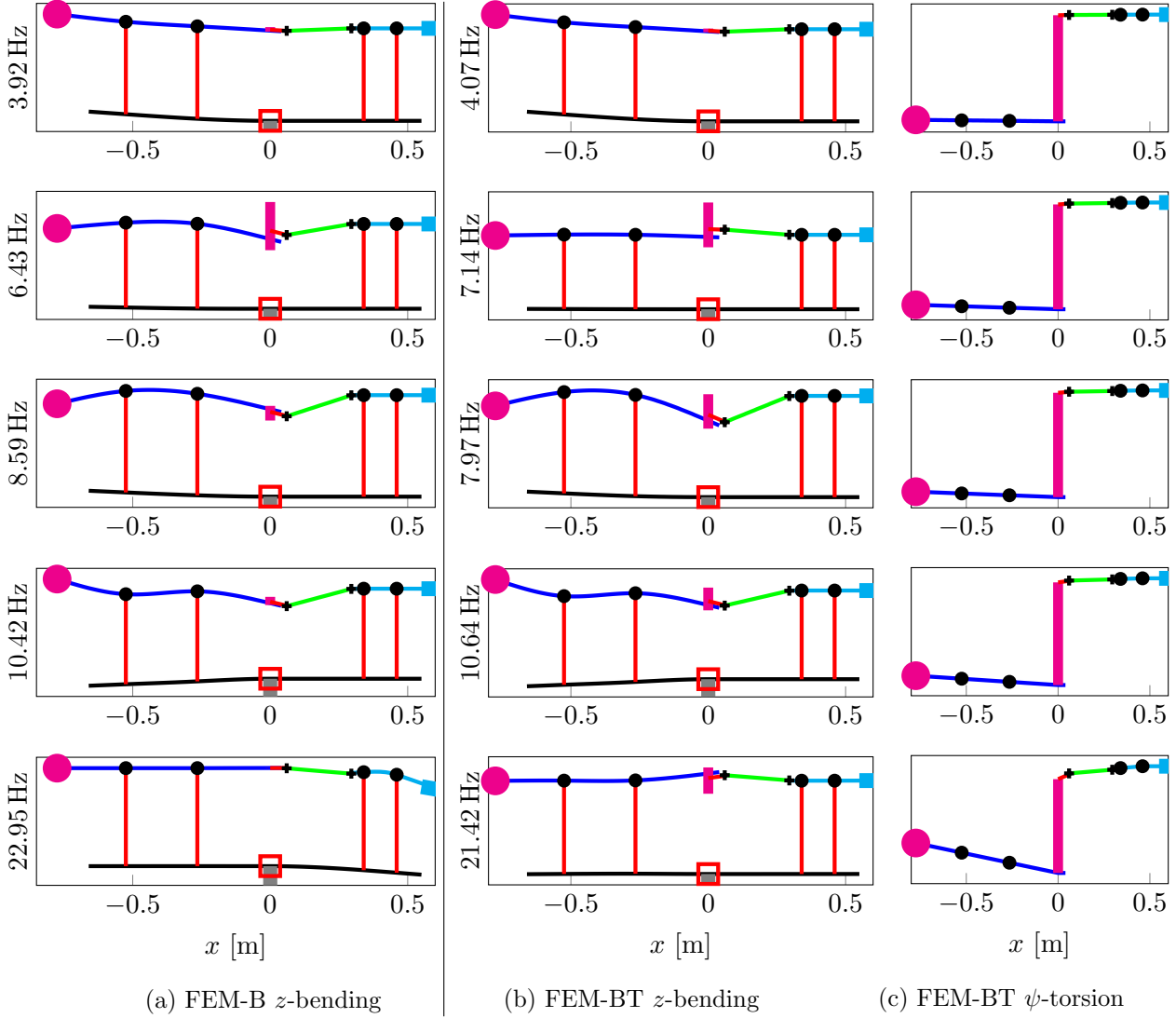


Figure 5.6: Schematic overview modeshapes bending and bending-torsion structural models with resonance frequencies  $\omega$ .

#### 5.2.4 Comparison between HIT and FEM modeshapes

Resonance frequencies from the HIT, bending model and bending-torsion model are summarized in table 5.1. As can be seen, the 'gearbox' modes between 6.0 Hz and 8.0 Hz are less accurately described by the bending model, while the bending-torsion model has Eigenfrequencies more close to the HIT results. An explanation can be the extra rotation stiffness and inertia of the shafts. Besides the resonance frequency, also the phase difference, shown in figure 5.4b, can be

Table 5.1: Resonance frequencies  $\omega$  [Hz] of the HIT, bending model and bending-torsion model.

Mode	HIT	Sweep	Bending	Bending-torsion
1	4.2	4.2	3.9	4.1
2	7.2	7.1	6.4	7.1
3	8.0	8.0	8.6	8.0
4	10.5	10.2	10.4	10.6

taken into account to verify the FEM model. The relative phase difference between the base and gearbox accelerometers of the first and fourth resonance frequency,  $0^\circ$  and  $180^\circ$  respectively, corresponds roughly to the modeshapes of the FEM model. However, the second and third

resonance frequency does not show the same relative phase difference between the base and gearbox accelerometers. An explanation for this can be the torsional excitation by the unbalance mass, which has a phase shift of  $90^\circ$  (see equation 1.2) compared to the force excitation by the unbalance mass.

Because the resonance frequencies of the bending-torsion FEM model corresponds better to the HIT compared to the bending FEM model, the bending-torsion model is used as structural model. However, the torsion is not measured directly via sensors, but extrapolated from the gearbox angle  $\eta$ . The extrapolation can be an inaccuracy of processing the accelerometer data with the structural model. This inaccuracy is hard to quantify, since the extrapolation is a solution to the under determined system of equations, having infinitely many solutions. The Matlab solver chooses one based on the minimal norm of the solution vector.

### 5.2.5 Model consistency

A FEM model is called consistent if the results are independent of the amount of used elements [32]. To check for consistency of the model, the resonance frequencies of the model are determined for several element lengths  $l$  in the range between 1000 mm and 20 mm. The resulting amount of elements is plotted with determined resonance frequencies in figure 5.7. As can be seen, the first, second, third and fourth Eigenfrequencies are stable after about thirty elements, which correspond to a mesh-size of 100 mm. The fifth Eigenfrequency is stable for a coarser grid with less elements, because this is the first linear torsion mode.

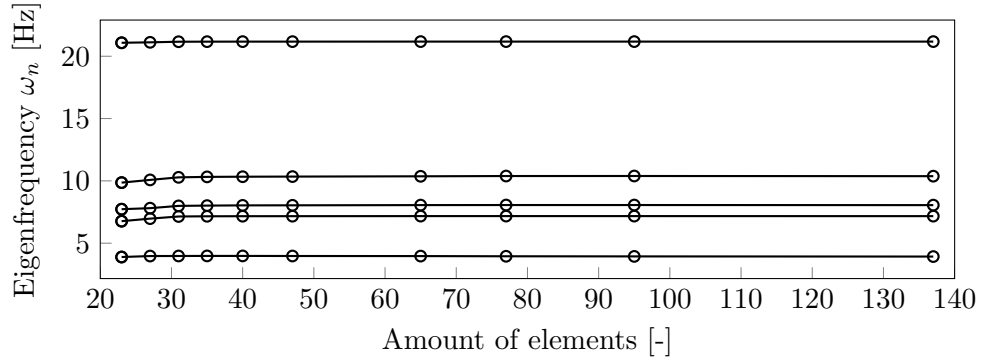


Figure 5.7: Eigenfrequencies for different amount of elements.

### 5.2.6 Damping

As was described in section 2.2.2, the damping parameter  $\beta$  can be determined from damping ratio  $\zeta$ . Figure 5.8 shows the response of accelerometer  $ac_1$  to the HIT. Using the 3 dB rule, indicated in the figure,  $\omega_1$  and  $\omega_2$  are roughly estimated to be 4.3 Hz and 4.5 Hz, respectively. Using equation 2.42 damping factor  $\zeta$  is determined 0.02. The SDoF system  $T(s)$  from equation 2.43 with estimated  $\zeta$  is added to figure 5.8 at the first resonance frequency to verify the damping ratio. As can be seen the damping ratio corresponds roughly to the test bench response. Choosing  $\zeta$  as 0.02 in equation 2.42 results for damping factor  $\beta$  as  $1.6 \times 10^{-3} \text{ rad}^{-1}$ .

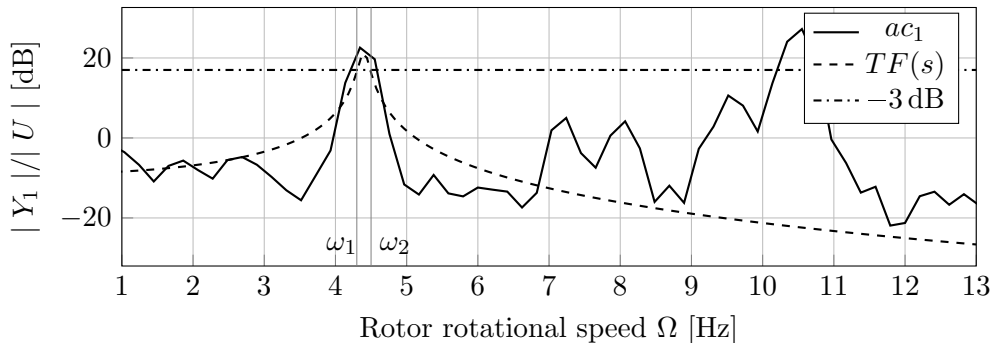


Figure 5.8: Estimation of damping ratio  $\zeta$  from peak width HIT accelerometer  $ac_1$ .

### 5.3 Predict accelerations using assumed rotor force

The reversed approach described in section 4.3 is applied to the test bench to quantify the prediction error. It is called reversed, because an assumed rotor load is used to predict the accelerations of test bench components. First this is done for one rotor speed, second it is done for a range of rotor speeds.

#### 5.3.1 Acceleration comparison for one specific rotational speed

The low-pass filtered measured accelerations from sensors  $ac_1$  till  $ac_5$  are compared to the prediction of the structural FEM model for a specific rotational speed. This comparison can be seen in figure 5.9. The blue line represents the prediction of the structural FEM model. The red line is the filtered acceleration measurement at  $\Omega_{LSS}$ . Additionally, also the HSS frequency  $\Omega_{HSS}$  filtered result is added to show its significance. As can be seen, the first two acceleration profiles

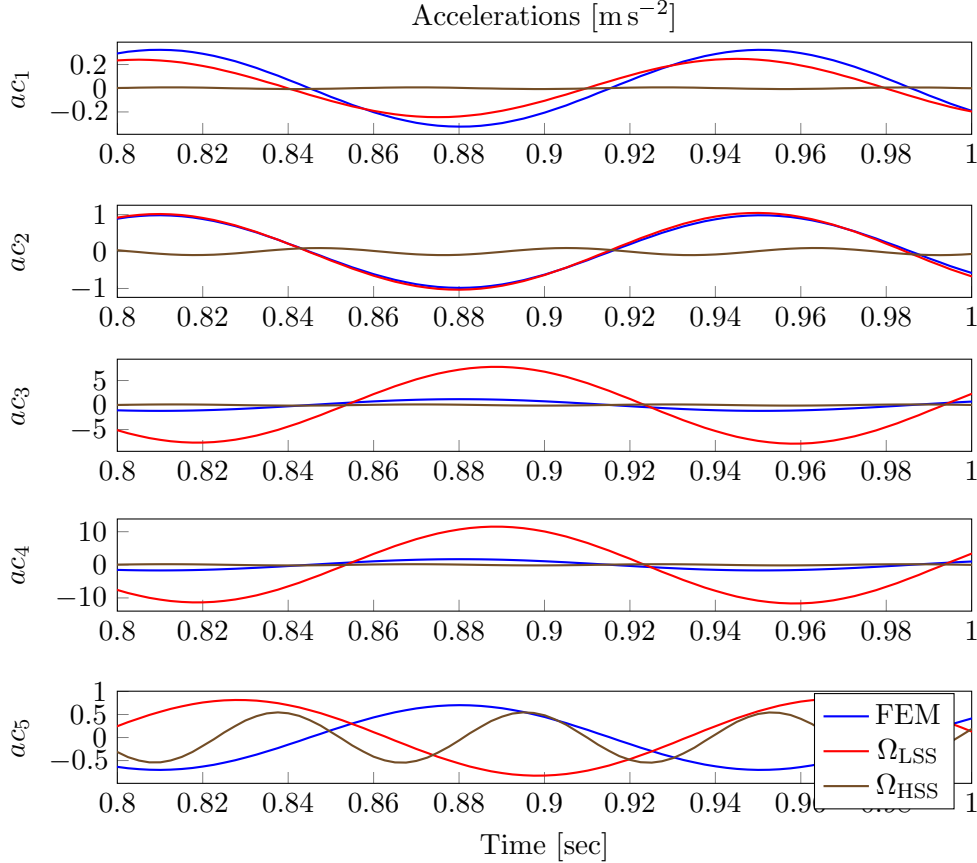


Figure 5.9: Comparison measured and predicted accelerations at 426 RPM rotor speed.

are quite similar. The third and fourth are predicted too low. The third and fourth sensor are far too low. This may indicate the structural model is not adequate at these sensors, which are located at the gearbox. For the fifth sensor, the HSS frequency is of significant influence.

#### 5.3.2 Acceleration comparison for a range of rotational speeds

The acceleration prediction and comparison for one constant rotational speed described in the previous section can be applied to a range of rotational speeds. To compare the prediction with real measurements, the amplitude of the prediction is divided by the amplitude of the measurement. So a perfect prediction has a comparison value of 1, indicated on the logarithmic  $y$ -axis by  $10^0$ . This is shown in figure 5.10 for the five accelerometers  $ac_1$  till  $ac_5$ . Also the resonance frequencies of the structural model  $\omega_{FEM}$  and the HIT  $\omega_{HIT}$  are included, shown by the vertical red and black lines. As can be seen, the comparison is not stable for any accelerometer over the frequency range. Especially before the first and between the second and third resonance frequency at 7.2 Hz and 8.0 Hz the prediction explodes. The prediction at frequencies between 4.5 Hz to 7.0 Hz and 8.5 Hz to 10 Hz are closer to the reference value 1 for  $ac_1$  to  $ac_4$ , but has



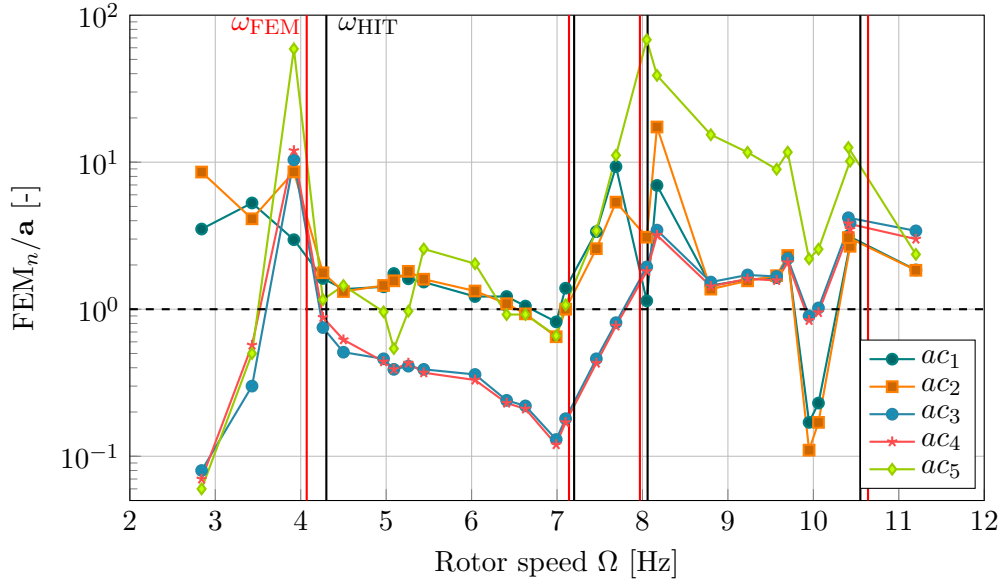


Figure 5.10: Acceleration comparison between the structural FEM model and five accelerometer measurements for a range of rotational rotor speeds  $\Omega$ , with the Eigenfrequencies  $\omega$  of the FEM and HIT drawn vertically, respectively.

far more than 2.15% error.  $ac_1$  and  $ac_2$  are mostly predicted larger than 1 while  $ac_3$  and  $ac_4$  is predicted to low between 4.5 Hz and 7.5 Hz. At 7.0 Hz and 8.0 Hz the gearbox is vibrating. Accelerometer  $ac_5$  shows an higher prediction error between 7.0 Hz to 10.0 Hz. This validation indicates a possible error in the inverse FEM model.

## 5.4 Load prediction using accelerations

Using the structural model with the algorithm described in section 4.2 the loads can be predicted using accelerometers as input. One of the loads is the rotor force due to the rotating unbalance. This force can be compared with the theoretical load described in equation 1.2. In this section, this is first described for one LSS rotational speed, afterwards it is applied to a range of rotational speeds.

### 5.4.1 Rotor load prediction at one constant rotational speed

The rotor and bearing loads can be predicted with the structural model, using equation 4.6. The rotor force in  $z$ -direction is shown in figure 5.11. The sinusoid line is the predicted force by the structural model, the dashed line is the theoretical rotor force by equation 1.2 due to the rotating unbalance mass. Acceleration  $\ddot{z}$  of the rotor origin is predicted also by the structural model and used in equation 1.2. As can be seen, the model prediction compared to the assumed maximum

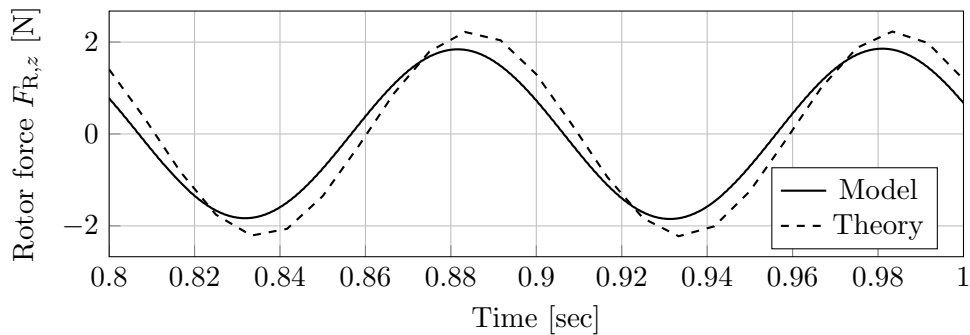


Figure 5.11: Rotor force in  $z$ -direction comparison between FEM and theoretical at 604 RPM rotor speed.

amplitude is almost the same for this rotational speed, but the error more than 2.15%.

### 5.4.2 Rotor force prediction for a range of rotational speeds

Figure 5.12 shows a comparison between the amplitude of the predicted rotor force and amplitude of the theoretical rotor force in  $z$ -direction for a range of rotational speeds based on equation 1.2. Ideally, this values should be 1, shown as black dotted line. The resonance frequencies of both the HIT ( $\omega_{\text{HIT}}$ ) and FEM model ( $\omega_{\text{FEM}}$ ) are shown as red and black vertical line, respectively.

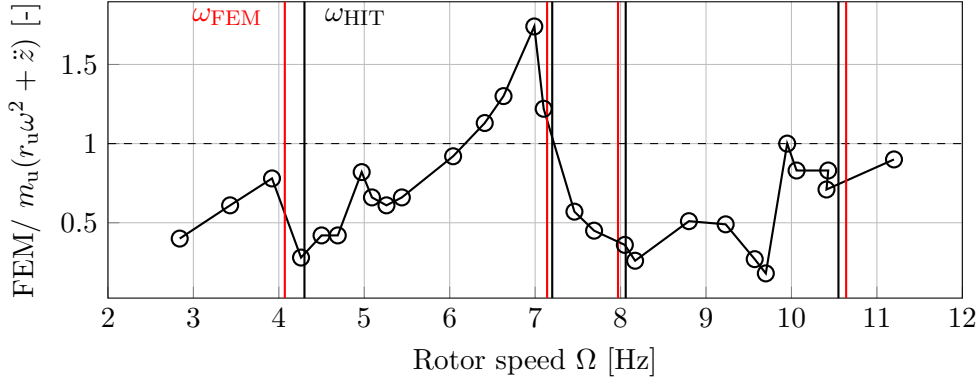


Figure 5.12: Comparison between FEM and theoretical rotor force for a range of rotational speeds  $\Omega$ , with the Eigenfrequencies  $\omega$  of the FEM and HIT drawn vertically, respectively.

As can be seen, the prediction is not stable at the ideal value 1. The first resonance frequency at 4.0 Hz of the FEM model is a bit too low compared to the HIT, this can explain the amplitude difference around this frequency. Between 4.5 Hz and 7.0 Hz the prediction also fluctuates. At the gearbox rotation modes of 7.0 Hz and 8.0 Hz, the FEM prediction is too low. This indicates the inverse FEM model is not correct.

## 5.5 Discussion

The resonance frequencies of the test bench are measured using an HIT and using a rotor speed sweep. These frequencies correspond with the Eigenfrequencies of a bending-torsion FEM model and partly with the analytic and Spacar models. Therefore these validation methods are assumed to be accurate. In literature also comparisons between Eigenfrequencies of both experiments and a structural model are done with accurate results, for example by Nigam et al. [43]. In general, the Eigenfrequencies are related the the ratio between stiffness and mass matrices, which seems to be correct according to the validations.

The modeshape amplitudes are related to the values of both the mass and stiffness matrices. From the accelerometer acceleration and rotor force predictions becomes clear that determining the modeshapes back using the inverse FEM method may be incorrect. This is indicated by the fact that both the predictions have a different error at the same frequencies. The acceleration prediction validation showed larger prediction errors compared to the rotor force validation approach.

As was observed as well from the analytical and Spacar, the gearbox modeshapes are sensitive to the gearbox spring, which may be modelled too simple by only a linear stiffness in axial direction. This can explain the wrong prediction at frequencies where the gearbox is vibrating. The FEM model is also sensitive to small changes of other parameters, for example point masses or lengths.

A comparison between the amplitude of experiments and a structural model is less common in literature. Wang et al. [44] uses an analytical based approach to predict the amplitudes of a clamped beam, but with an error of 20 - 30%. Gherlone et al. [45] uses an inverse FEM approach to predict motion with strain measurements applied to a clamped beam with an load prediction error about 5.9%. Kawai et al. [46] poses the inverse FEM and describes it as inaccurate very sensitive to measurement noise. Dividing the measured accelerations by the rotational speed squared also results in small displacement values, which are sensitive to noise. The inverse of the dynamic stiffness matrix is ill posed due to the small amount of measurement nodes. The displacement sensitivity and the ill posed inverse can both result in an inaccurate solution.

## 6 Outlook

In this section, acceleration measurements are used as input for the structural FEM model to predict internal loads at a specific constant LSS rotational speeds. This is done as outlook to a possible application of the structural model. The prediction is done at several rotational speeds to see the influence of the speed on the internal loads, for example the bearing loads. At resonance frequencies where the test bench is vibrating, higher dynamic loads are expected. The prediction is done to show the possible practical use of the proposed structural model.

### 6.1 Prediction at one constant rotational speed

First, coordinates  $q$ , containing bending and torsional deflection, are predicted using the structural model, according to the algorithm described in section 4.2. The displacements and shaft rotations are visualized in a schematic overview of the test bench in figure 6.1. The rotor is shown at the left side as magenta disc, the generator at the right side as cyan rectangle. The tower is located at the red square mark with grey line at (0,0). The acceleros are visualized as orange square marks. The used damping coefficient  $\beta$  is  $1.6 \times 10^{-3} \text{ rad}^{-1}$  and the number of beam elements is 362. The  $x$ -rotation of the gearbox is shown by  $\eta$ . The displacements in  $z$ -direction are shown in figure 6.1a, the shaft rotation  $\psi$  due to torsion and gearbox rotation is shown figure 6.1b. As can be seen, the gear ratio causes a vertical jump in rotation (magenta line), appointed with an arrow. This rotation is due to the rigid body motion of the gearbox. The torsion inclination of the blue LSS and green INT are slightly opposite to each other, as is expected by a one-stage gearbox. The shapes are similar to the modeshape of the model, as already shown in figure 5.6. Based on figure 5.10, the acceleration prediction of the gearbox sensors  $ac_3$  till  $ac_5$  is too low and should have a much higher amplitude. Figure 6.2 shows the

(a) Displacement prediction

(b) Shaft torsion prediction

Figure 6.1: Displacement and shaft rotation prediction at 604 RPM. *If the figure does not appear interactive, please enable this function and click on it or use a recent version of Adobe Reader.*

internal force in  $z$ -direction in the bearing (spring) elements (main bearings). As expected, they are opposite to each other due to the bending moment in the shaft. The force amplitude of the bearings differs a bit. The frequency corresponds to the LSS rotational speed. At this frequency, the accelerometer validation had an error of about 10% and the rotor validation an error of 20%, as was shown in figures 5.10 and 5.12, respectively. Therefore this bearing load prediction should be considered with such an error.

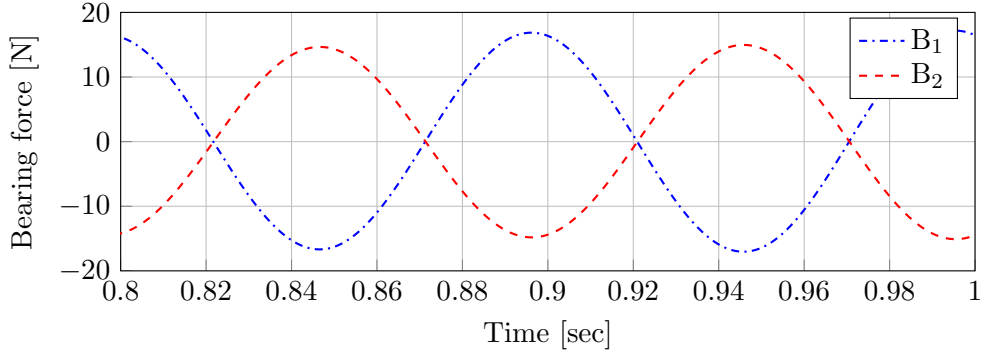


Figure 6.2: Bearing load prediction at 604 RPM.

## 6.2 Bearing load prediction for a range of rotational speeds

The prediction of rotor and bearing loads is done for a range of rotational speeds containing four modelled resonance frequencies. In figure 6.3 the amplitude of the main bearings is shown for a range of rotational speeds. For an higher frequency the load increases globally. At the resonance frequencies corresponding to figure 5.6 peaks can be observed at 4.0 Hz, 7.0 Hz and 10.0 Hz. The resonance frequency of 8.0 Hz is merely visible. This is explained by figure 5.6 where can be seen that this is a gearbox rotation mode.

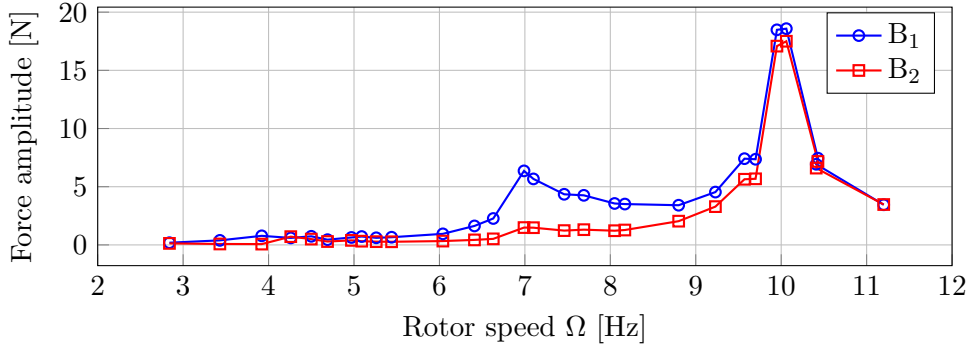


Figure 6.3: Bearing load prediction for a range of rotational speeds.

Because of the validation done in section 5.3 and 5.4, the bearing loads prediction should be considered with the errors shown in figures 5.10 and 5.12. This means the force prediction of the bearings is at all speeds considered not reliable. But even with this prediction error the influence of the vibrations on the bearing loads is clearly visible.

## 7 Conclusion

A feasibility study to a simple and fast structural model of a test bench is made to process measurements from accelerometers to internal loads. The dimensions of the test bench are designed to vibrate by an rotating unbalance, since at resonance frequencies, the dynamic loads can be significantly higher compared to the quasi-static load case. The research questions are stated and answered as follows:

### **How can an analytic structural modal be defined and applied to a wind turbine?**

An analytic structural model considering the low speed part of the drive train is defined. This is done by using multiple beam sections connected by boundary conditions. Linking multiple beams together leads to a complex formulation for the modeshape scaling, making it not suitable to use. Also, damping at resonance frequencies is important, which is not taken into account in the analytic model. This results in an infinite excitation at resonance frequencies.

### **How can a numerical structural model be defined and applied to a wind turbine?**

The first considered numerical model is the Finite Element Method (FEM) using the program Spacar. This enables a simple and fast formulation of different beam elements describing bending and torsion in 3D. The node numbering is done internally in the program; mass and stiffness matrices cannot easy be manipulated to use them for acceleration input. Additionally, details like the gearbox ratio can not be added.

The second considered numerical model is a manual defined FEM model. This enabled a simple and fast formulation of different beams in 2D including bending in  $z$ -direction and shaft torsion. Gearbox details, for example the gear ratio, were added using the Lagrange multiplier theorem.

### **What manipulation is needed to use the structural model for measurement processing?**

First the acceleration measurement data is detrended to remove an acceleration offset. Second, the data is filtered using a bandpass filter to remove noise and higher harmonic frequencies. Third, the mass and stiffness matrices of the structural model are manipulated according to known and unknown coordinate or load values using an inverse finite element method.

### **What is the accuracy of the structural model?**

The model was validated using three approaches. The first approach was by using a hammer impact test on the test bench and comparing its resonance frequencies with the Eigenfrequencies of the FEM model. From this the necessity of including both bending and torsion in the model became clear, because this model had the most similar resonance frequencies. A rotor speed sweep is done to validate the use of non rotating beams to represent the rotating shafts. Both have similar resonance frequencies.

The second validation assumed a theoretical harmonic rotor excitation force as input for the model. Accelerations were predicted with the structural model and compared with accelerometer measurements. This validation showed a considerable difference between model predictions and measurements, especially low-frequent and at the gearbox resonance frequencies. Between 5.0 Hz and 7.0 Hz the prediction seemed more stable, but still with a relatively large error.

The third validation used acceleration measurements to predict the rotor excitation force. This was done at several constant rotational speeds of the rotor. At most rotor speeds the rotor force prediction is too low with about 50% error. At 7.0 Hz the prediction is too high with an error of 60%.

### **To what extent can internal loads, moments and torques of a wind turbine be determined using accelerometers?**

Acceleration measurements are used as input to a structural model to predict the motion and loads. However, the validation showed prediction with significant errors at most frequencies. Therefore the set requirement of 2.15% prediction error is not met at any speed in the range of

the first four resonance frequencies of the test bench. The (inverse) FEM model appears to be sensitive to small changes of test bench dimensions which makes it not suitable to validate the structural model. Also the test bench has too much uncertainties to be accurately represented in a model.

Although the prediction is not accurate, the simple analytic and numerical modelling of the drive train gives insight in the governing dynamics of a complex system with multiple bodies.

## 8 Recommendations

The current structural model does not show stable and reliable force predictions for a frequency range in the first four modes. The first recommendation is to use a simple test set-up like a clamped beam or mass-spring system as proof of principle to validate the inverse finite element method using accelerometers as input. Preferably the exciting load or displacement is directly measured. The current test bench is too complex to prove the principle of the inverse structural model.

The second recommendation is to circumvent the inverse model. This can be done by the use of known harmonic input rotor forces and moments to predict the test bench motion for different speeds. The measured accelerations can be matched to the motion shape, resulting in a corresponding rotor force. This is an optimization problem instead of an inverse solution problem.

The third recommendation is to add rotational measurements. The load prediction can be improved by using a rotational encoder to measure torsion of shafts. As became clear of the FEM model modes, shaft rotation has to be taken into account to describe the gearbox modes accurately. However, shaft rotations are currently not measured at the test bench, resulting in an under determined set of equations to solve in the structural model. In practise, this means an infinite amount of solutions for the shaft rotation, where the algorithm picks a single one. This solution depends on the used solver routine. The easiest location to put the rotational encoders is at the driving DC motor and DC generator.

The last recommendation concerns test bench uncertainty of the gearbox spring. Its stiffness is unknown and no data-sheets are available. The spring is not only loaded axially as linear movement, but also radial in  $x$  and  $y$ -direction during rotational movement of the gearbox. Because the spring is clamped at both sides this rotational stiffness is hard to determine. The clamping causes also extra forces in case the gearbox is not properly aligned with the base. A solution for this stiffness uncertainty can be the use of a folded leafspring, which stiffness are easier to determine. Two schematic sketches are shown in figure 8.1 with the gearbox attached to the base by a leafspring. Figure 8.1a only allows for  $z$ -bending, while figure 8.1b allows for both  $z$  and  $y$ -bending.

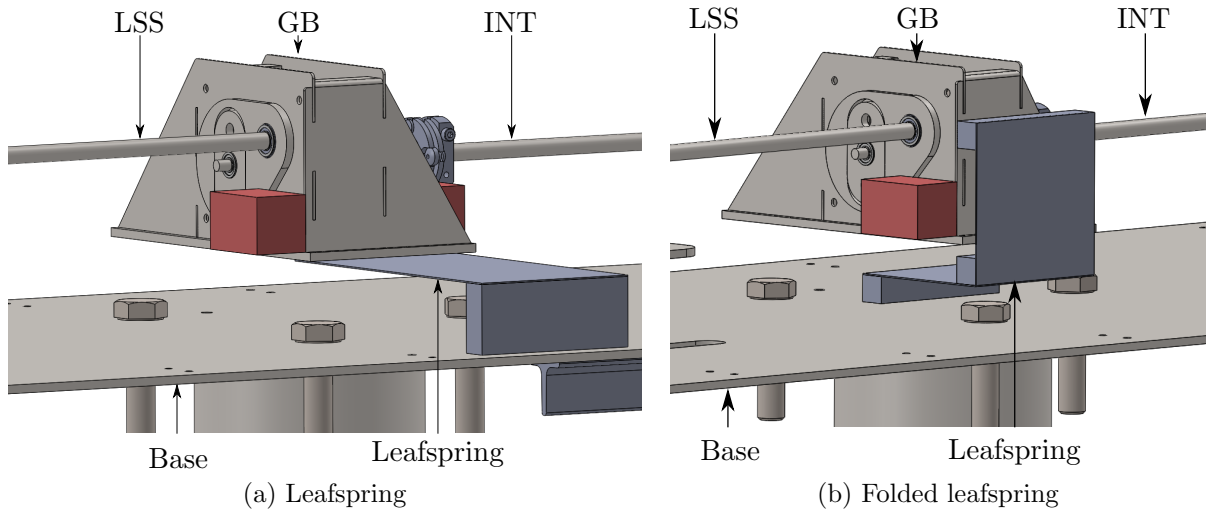


Figure 8.1: Two leafspring configurations between the gearbox and base





# Bibliography

- [1] Bible, *King James Version*. 1611. John 1.
- [2] IRENA, “Renawable power generation costs in 2017.” [https://www.irena.org/-/media/Files/IRENA/.../IRENA\\_2017\\_Power\\_Costs\\_2018.pdf](https://www.irena.org/-/media/Files/IRENA/.../IRENA_2017_Power_Costs_2018.pdf), 2017. [Online; accessed 11-April-2018].
- [3] P. S. Veers and S. Butterfield, “Extreme load estimation for wind turbines: Issues and opportunities for improved practice,” 2001.
- [4] T. Tinga, *Principles of Loads and Failure Mechanisms*. Springer, 2013. DOI: 10.1007/978-1-4471-4917-0.
- [5] NREL, “Gearbox reliability collaborative research.” <https://www.nrel.gov/wind/grc-research.html>. [Online; accessed 16-November-2018].
- [6] S. Mulski, “Load calculations for wind turbines.” [http://www.simpack.com/fileadmin/simpack/doc/newsletter/2014/March\\_2014/Spreads/SN-1-Mar-2014\\_SIMPACK\\_Wind-Turbines\\_Load-Calculation\\_HRes\\_spreads.pdf](http://www.simpack.com/fileadmin/simpack/doc/newsletter/2014/March_2014/Spreads/SN-1-Mar-2014_SIMPACK_Wind-Turbines_Load-Calculation_HRes_spreads.pdf), March 2014. [Online; accessed 11-April-2018].
- [7] J. Peeringa, “Comparison of extreme load extrapolations using measured and calculated loads of a mw wind turbine,” 2009.
- [8] T. Ishihara, H. Ishii, and M. Nishio, “Maximum wind loads on a wind turbine under operating conditions.” [windeng.t.u-tokyo.ac.jp/ishihara/proceedings/2011-1\\_poster.pdf](http://windeng.t.u-tokyo.ac.jp/ishihara/proceedings/2011-1_poster.pdf). [Online; accessed 11-April-2018].
- [9] D. P. Rommel, “Prediction of failures in wind turbine components based on physical models.” submitted April 2018, October 2016.
- [10] F. P. G. Márquez, A. M. Tobias, J. M. P. Pérez, and M. Papaelias, “Condition monitoring of wind turbines: Techniques and methods,” *Renewable Energy*, vol. 46, pp. 169 – 178, 2012.
- [11] b. S. Kuseyri, “Condition monitoring of wind turbines: Challenges and opportunities,” 06 2015.
- [12] T. W. Verbruggen, “Load monitoring for wind turbines.” <https://www.ecn.nl/publications/PdfFetch.aspx?nr=ECN-E--09-071>. [Online; accessed 11-April-2018].
- [13] “Condition monitoring and fault detection of wind turbines and related algorithms: A review,” *Renewable and Sustainable Energy Review*.
- [14] F. Wasilczuk, R. Gawarkiewicz1, and M. Wasilczuk, “Drivetrain of a wind turbine,” *Machine Dynamics Research*, vol. 39, 2015.
- [15] M. Froese, “What are the new ideas in condition monitoring for wind turbines?.” <https://www.windpowerengineering.com/business-news-projects/new-ideas-condition-monitoring-wind-turbines/>, 2017. [Online; accessed 12-April-2018].
- [16] V. L. Jantarajunior, H. Basoalto, H. Dong, F. P. G. Marquez, and M. Papaelias, “Evaluating the challenges associated with the long-term reliable operation of industrial wind turbine gearboxes,” vol. 454, 2018.
- [17] SKF, “Bearing calculation.” <https://www.skf.com/binary/49-62749/RTB-1-05-Bearing-calculation.pdf>. [Online; accessed 16-January-2019].

- [18] D. P. Rommel, "Load calculation at low and high speed gearbox shafts." submitted April 2018.
- [19] W. T. Latt, C. Y. Shee, C. N. Riviere, and W. T. Ang, "Estimating displacement of periodic motion with inertial sensors," *IEEE SENSORS JOURNAL*, vol. 8, 2008.
- [20] S. Lopez-Querol, L. Cui, and S. Bhattacharya, "Numerical methods for ssi analysis of off-shore wind turbine foundations," *Wind Energy Engineering, Elsevier*, vol. 39, 2017.
- [21] F. P. G. Márquez, J. M. P. Pérez, A. P. Marugán, and M. Papaelias, "Identification of critical components of wind turbines using fta over the time," *Renewable Energy*, vol. 87, pp. 869–883, 2016.
- [22] D. P. Rommel, D. D. Maio, and T. Tinga, "Calculating wind turbine component loads for improved life prediction." submitted December 2018, December 2018.
- [23] Romax technology, "Wind turbine drivetrain technology and cost drivers." [https://community.dur.ac.uk/supergen.wind/docs/presentations/4th\\_Seminar\\_Presentations/JohnCoultrate\\_Romax.pdf](https://community.dur.ac.uk/supergen.wind/docs/presentations/4th_Seminar_Presentations/JohnCoultrate_Romax.pdf), 2011. [Online; accessed 13-April-2018].
- [24] Lagerwey, "Unique direct drive generator." <https://www.lagerweywind.com/technology/>, 2015. [Online; accessed 12-April-2018].
- [25] H. Alberg, "Analytical solution for eigenvalues of a rotating timoshenko beam." [http://rmseura.tkk.fi/rmllehti/1981/nro3/RakMek\\_14\\_3\\_1981\\_3.pdf](http://rmseura.tkk.fi/rmllehti/1981/nro3/RakMek_14_3_1981_3.pdf). [Online; accessed 4-February-2019].
- [26] J. P. Schilder, *DYNAMICS 2*. Univeristy of Twente, 2014. Dictaat 065 - 115714.
- [27] R. Tiwari, *Rotor Systems: Analysis and Identification*. 12 2017. ISBN:9781138036284.
- [28] J. L. Meriam and L. G. Kraige, *Engineering Mechanics Dynamics*. Virginia Polytechnic Institute and State University, 2012. Seventh edition.
- [29] G. Takacs and B. Rohal-Ilkiv, "Model predictive vibration control efficient constrained mpc vibration control for lightly damped mechanical structures," 2012. ISBN: 978-1-4471-2332-3.
- [30] R. G. K. M. Aarts, "Spacar 2015 - main introduction." [https://www.utwente.nl/en/et/ms3/research-chairs/WAoud\\_niets\\_uit\\_wissen\\_aub/software/spacar/2015/intro/#copyright](https://www.utwente.nl/en/et/ms3/research-chairs/WAoud_niets_uit_wissen_aub/software/spacar/2015/intro/#copyright). [Online; accessed 19-November-2018].
- [31] R. G. K. M. Aarts, J. B. Jonker, and J. v. Dijk, "Prototype modelling of mechanical systems, an introduction for module 7&8," 2015.
- [32] R. D. Cook, D. S. Malkus, M. E. Plesha, and R. J. Witt, *Concepts and Applications of Finite Element Analysis*. USA: John Wiley; Sons, Inc., 2007. ISBN:0470088214.
- [33] J. P. Schilder, *DYNAMICS 3 - Flexible multibody dynamics*. Univeristy of Twente, 2015.
- [34] R. Ferrero, F. Gandino, and M. Hemmatpour, "Exploiting accelerometers to estimate displacement," *Embedded Computing (MECO)*, 2016. 10.1109/MECO.2016.7525741.
- [35] J. Bianchi, E. Balmes, G. Vermot des Roches, and A. Bobillot, "Using modal damping for full model transient analysis. application to pantograph/catenary vibration,"
- [36] H. Tjrdeman and A. Boer, *Structural vibrations*. Univeristy of Twente, 2005.
- [37] RS-online, "Radial ball bearing." <https://nl.rs-online.com/web/p/ball-bearings/6126063/>. [Online; accessed 19-November-2018].
- [38] RS-online, "Spurs gears 1.0mod 20° p.a.." <https://docs-emea.rs-online.com/webdocs/157a/0900766b8157a706.pdf>. [Online; accessed 11-December-2018].

- [39] J. S. Wu and C. H. Chen, “Torsional vibration analysis of gear-branched systems by finite element method,” *Journal of Sound and Vibration*, vol. 240, no. 1, pp. 159–182, 2001.
- [40] Matlab, “Detrend documentation.” <https://www.mathworks.com/help/matlab/ref/detrend.html>. [Online; accessed 28-December-2018].
- [41] R. G. K. M. Aarts, *System Analysis and Control*. Univeristy of Twente, 2015.
- [42] Matlab, “Filtfilt documentation.” <https://nl.mathworks.com/help/signal/ref/filtfilt.html>. [Online; accessed 17-December-2018].
- [43] N. V. Oza and R. D. Patel, “Predicting dynamic behavior of cantilever beams using fea and validating through ema,” *IJJERT*, vol. 3, 2014.
- [44] B.-T. Wang and K.-Y. Lin, “Prediction of harmonic force acting on cantilever beam,” 01 2019.
- [45] M. Gherlone, P. Cerracchio, M. Mattone, M. Di Sciuva, and A. Tessler, “An inverse finite element method for beam shape sensing: Theoretical framework and experimental validation,” *Smart Materials and Structures*, vol. 23, p. 045027, 03 2014.
- [46] T. Kawai, H. Ota, M. Ito, and T. Ohyama, “- parameter identification of beam using image processing 2nd report, in the case of non-uniform beam,” in *Inverse Problems in Engineering Mechanics* (M. Tanaka and G. S. Dulikravich, eds.), pp. 235 – 242, Oxford: Elsevier Science Ltd, 1998.
- [47] M. . C. DRILLS, “980d series 35mm single ratio metal gearbox (central output shaft).” <https://docs-emea.rs-online.com/webdocs/0bf3/0900766b80bf315c.pdf>. [Online; accessed 19-November-2018].
- [48] RS-online, “Pillow block bearing 12mm id.” <https://nl.rs-online.com/web/p/bearing-units-plummer-block-accessories/7508933/>. [Online; accessed 20-November-2018].
- [49] ALTRA INDUSTRIAL MOTION, “Huco dynatork flexible couplings.” <https://docs-emea.rs-online.com/webdocs/14a0/0900766b814a0492.pdf>. [Online; accessed 19-November-2018].
- [50] P. Dvorak, “What is the job of a coupling in a wind-turbine drivetrain?” <https://www.windpowerengineering.com/mechanical/couplings/job-coupling-wind-turbine-drivetrain/>. [Online; accessed 30-November-2018].



# A Test bench description

This chapter describes the used test bench. First the design is shown and in the second section all relevant dimensions are given.

## A.1 Design

A test bench is built to verify a structural model. The base frame and shafts are considered flexible. Figures A.2 and A.3 show the CAD design from different perspectives with components described below, where the numbers correspond to the ones in the pictures.

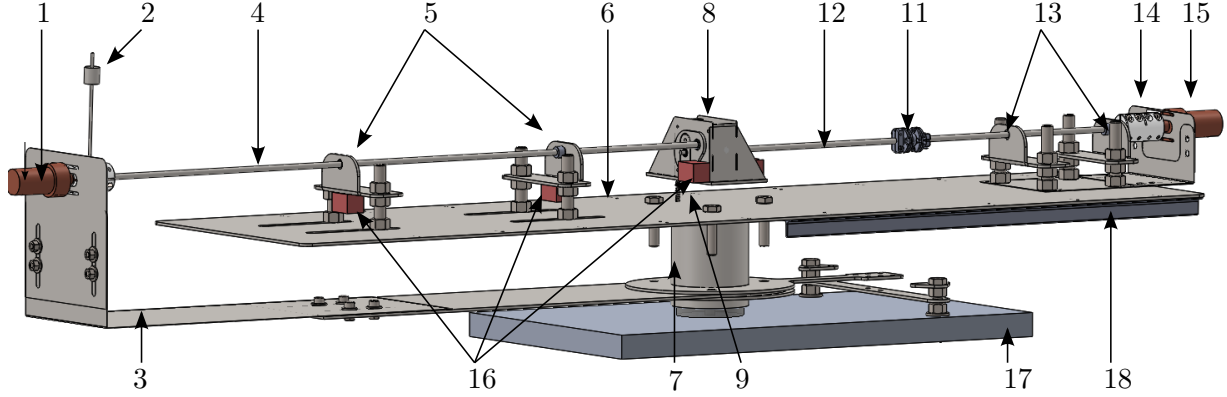


Figure A.1: CAD model test bench 3D view, *in corporation with D. Berendsen.*

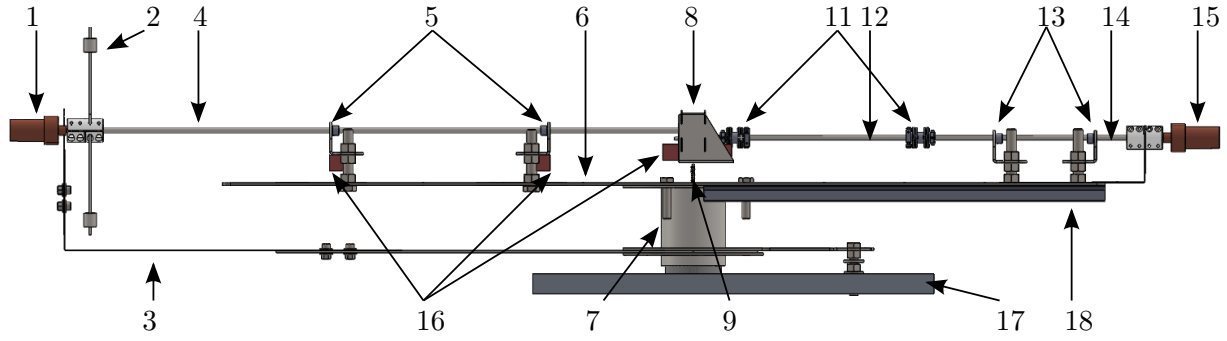


Figure A.2: CAD model test bench side view XZ plane, *in corporation with D. Berendsen.*

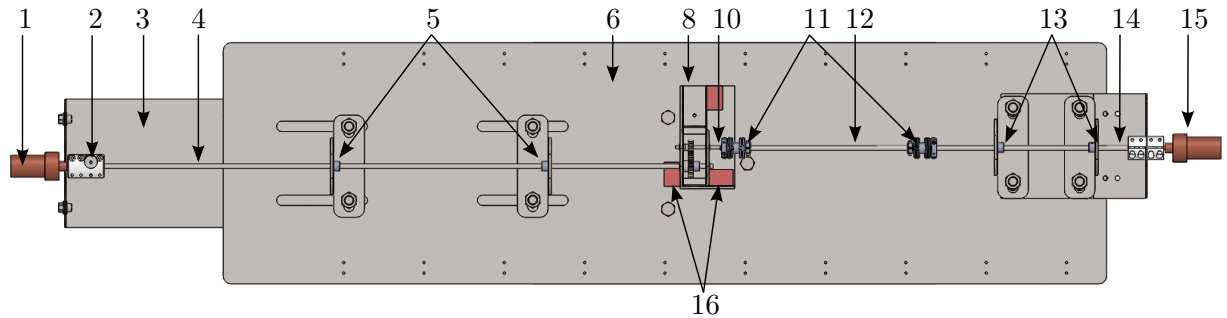


Figure A.3: CAD model test bench top view XY plane, *in corporation with D. Berendsen.*

1. A DC motor drives the 'rotor' and is supported by a leafspring 'DC motor support'. It has a speed range of about 180 RPM till 950 RPM, with a maximum voltage of 15 V [47].
2. The varying wind load is modelled by two unbalance masses. Its radii can be varied. They are mounted on a rigid coupling which couples the DC drive shaft to the LSS.
3. The DC motor is supported by a folded leafspring as counter torque.
4. A shaft with diameter 6.0 mm is used as LSS.

5. Two ball bearings are used as main bearings [37]. To mimic viscous friction a more heavy industrial alternative was considered [48], but the viscous friction absorbed too much power of the DC motor, as was observed in practise.
6. The flexible base frame is modelled as a sheet, the rear part below the generator is stiffened by two stiffeners.
7. The tower, with certain stiffness about the z-axis to model the tower stiffness, realized by springs for the test bench.
8. The gearbox ratio  $R_i$  is chosen as 2.45 and assembled in house using two POM gears. The gears have a pitch of 15.0 mm and 36.0 mm, respectively. The shafts are both connected by two bearings to the gearbox. It is modelled by a box with a thick bottom plate, screwed together.
9. The gearbox is supported by a spring to the base frame.
10. A short shaft with diameter 4.0 mm is used as HSS.
11. Two membrane couplings [49]. Real wind turbines use metal disc packs. Both are shown in figure A.4. In figure A.4a the flexible membranes can be seen, which are needed to compensate for misalignment between the gearbox and generator shaft. They act as radial and bending spring, causing extra forces on the bearings. Figure A.4b shows the one used in the test bench. Cardanic-couplings are not used in practise because of extra rotating parts and costs.
12. An intermediate shaft with diameter 6.0 mm is used between the membrane couplings.
13. Two generator bearings supporting the generator shaft [37].
14. A generator shaft with diameter of 6.0 mm is used between the membrane coupling and the generator
15. The generator is modelled by a DC motor [47]. The voltage output can be measured via a voltage divider using Labview. It has an internal transmission with a ratio of 6:1. It is coupled to the generator shaft by a rigid coupling.
16. Since the bending curve of a beam is of fourth order, at least four accelerometers for the LSS in combination with the base frame are used [18]. To measure the torsion fluctuation two accelerometers are placed on the XY plane of the gearbox. The shafts are assumed torsion rigid, because shaft rotations are not measured. All accelerometers measure in 3D starting from 0.0 Hz, so without frequency offset. The locations are chosen with aid of the modeshapes to measure at five non-singular locations.
17. The test bench rests on a solid aluminium ground plate.
18. The base frame can be stiffened by extra T profiles.



(a) Metal discpack coupling wind turbine, from [50]. (b) Membrane coupling test bench, from [49].

Figure A.4: Couplings between gearbox and generator

## A.2 Dimensions and properties test bench

Loads due to dynamic excitation can be significantly higher in comparison to static loading, especially at resonance frequencies. Therefore the dimensions and masses of the test bench

are chosen in such a way that they are in the range of the DC motor speed. As can be seen in figure A.3, the positions of the bearings can be shifted through slots to vary the resonance frequencies in a small range. The analytic approach described in section 2.1 is used to estimate the Eigenfrequencies based on dimensions. All used dimensions and properties are listed:

Table A.1: Used steel properties.

Symbol	Parameter	Value	Unit
$E$	E-modulus	210	GPa
$G$	G-modulus	70	GPa
$\rho$	Density	$7.8 \times 10^3$	kg m <sup>3</sup>

Table A.2: Main lengths.

Symbol	Parameter	Value	Unit
$l_r$	Rotor - Bearing 2	250	mm
$l_s$	Bearing 2 - Bearing 1	260	mm
$l_p$	Bearing 1 - Tower	265	mm
$l_{be}$	Bearing 2 - free end base	135	mm
$l_{gbx1}$	GB LSS side - Tower	40	mm
$l_{gbx2}$	GB HSS side - Tower	30	mm
$l_{GB}$	Gearbox y length	128	mm
$l_{HSS}$	HSS	60	mm
$l_{INT}$	INT	235	mm
$l_{g1}$	Coupling 2 - Bearing 3	45	mm
$l_{g2}$	Bearing 3 - Bearing 4	120	mm
$l_{g2}$	Bearing 4 - Generator	90	mm
$l_{GEN}$	Generator	70	mm
$h_b$	Base - LSS	55	mm
$r1r2$	LSS - HSS	23.5	mm

Table A.3: Cross section dimensions.

Symbol	Parameter	Value	Unit
$R_{LSS}$	LSS radius	3	mm
$R_{HSS}$	HSS radius	2	mm
$R_{INT}$	INT radius	3	mm
$w_{bf}$	Base width	300	mm
$t_{bf}$	Base thickness	3	mm
$r_{on}$	Rotor unbalance radius	5	mm
$w_{GB}$	Gearbox width	70	mm
$t_{GB}$	Gearbox thickness	7	mm

Table A.4: Stiffness parameters.

Symbol	Parameter	Value	Unit
$k_{DC}$	DC motor support	141.3	N m <sup>-1</sup>
$k_b$	Bearing	$190 \cdot 10^6$	N m <sup>-1</sup>
$k_{GB}$	Gearbox linear spring	$2.2 \cdot 10^3$	N m <sup>-1</sup>
$k_{GB,\theta}$	Gearbox rotation spring	0.13	N m <sup>-1</sup>
$k_{C,r}$	Membrane radial coupling	4.0	kN m <sup>-1</sup>
$k_{C,\theta}$	Membrane angular coupling	0.3	Nm/°
$k_{C,\psi}$	Membrane torsion coupling	145	N m rad <sup>-1</sup>

Table A.5: Mass properties.

Symbol	Parameter	Value	Unit
$m_r$	Rotor mass	0.485	kg
$J_{r,\theta}$	Rotor mass inertia $y$ -axis	$8.2 \times 10^{-4}$	$\text{kg m}^2$
$J_{r,\psi}$	Rotor mass inertia $x$ -axis	$5.0 \times 10^{-4}$	$\text{kg m}^2$
$m_b$	Bearing holder mass	0.602	kg
$J_{b,\theta}$	Bearing holder mass inertia $y$ -axis	$142 \times 10^{-6}$	$\text{kg m}^2$
$m_{GB}$	Gearbox mass	0.580	kg
$J_{GB,\theta}$	Gearbox mass inertia $y$ -axis	$410 \times 10^{-6}$	$\text{kg m}^2$
$m_A$	Accelerometer mass	40	g
$J_{A,\theta}$	Accelerometer mass inertia $y$ -axis	$2.6 \times 10^{-6}$	$\text{kg m}^2$
$m_C$	Membrane coupling mass	14	g
$J_{C,\theta}$	Membrane coupling mass inertia $y$ -axis	$60 \times 10^{-8}$	$\text{kg m}^2$
$J_{C,\psi}$	Membrane coupling mass inertia $x$ -axis	$60 \times 10^{-8}$	$\text{kg m}^2$
$J_{LSS}$	LSS gear mass inertia $x$ -axis	$1.4 \times 10^{-6}$	$\text{kg m}^2$
$J_{HSS}$	HSS gear mass inertia $x$ -axis	$4.5 \times 10^{-8}$	$\text{kg m}^2$

Table A.6: Other properties.

Symbol	Parameter	Value	Unit
$R_i$	Ratio Gear 1 / Gear 2	2.45	-



# B Matlab program description

This chapter gives a short documentation of the used Matlab files.

## B.1 Parameters definition

All relevant dimensions, as stated in section A.2, are also described in the Matlab file *parameters.m*. This file is used for the analytic, Spacar and manual FEM structural models.

## B.2 Analytic model

The Matlab file defines the analytic model. First the cross sections are defined by the area and inertia. The relative lengths between each node are converted to an absolute coordinate system with  $x$  zero at the tower.

The shape functions for each beam section are defined as symbolic functions, which are differentiated to the angle, moment and shear force. The boundary conditions are applied which results in a 24x24 matrix to solve for the eigenvalue. The modeshapes are obtained by inserting the found eigenvalue and choosing the free scaling factor as 1. Four modeshapes are plotted and saved as .svg and .csv file.

## B.3 Spacar

The Spacar model uses the extended version 2017 of Spacar. The dimensions are defined from the parameters.m file. The model is build in 3D. The inertias and stiffnesses are defined for the different cross sections. The properties for the springs and bearings are overridden.

The model is build from the tower, connecting each beam element section to each other by the displacements and rotations. Constraints with the ground are added. Gravity can be added. Colours are added manually for Spavisual. Modeshape results are visualized in Spavisual and can be manually exported.

## B.4 FEM

The manual defined FEM program has two versions: one with only bending and one with bending and torsion. Both are defined in the same way. First the model is defined. Second the acceleration data is preprocessed. Last the model can be manipulated to be used in two ways: to predict rotor force or to predict accelerations.

### B.4.1 Model

The area and inertia are defined per beam section in Matlab cells. Relative beam section lengths are converted to an absolute coordinate system with  $x$  is zero at the tower. The complete test bench is defined using beam elements. The  $x$ -nodes per element (Base, LSS, etc.) are defined using the given lengths. Beam elements are defined between  $x$ -nodes.

The nodes defined by the user are converted to program indices, since a node can have multiple indices (displacement, rotation, etc.). To check the dimension input a undeformed plot is drawn with all elements and added details.

With the defined dimensions for each element the mass and stiffness matrices are determined and stored in a 3D Matlab cell. The different element matrices are linked to each other by the bearing and coupling stiffnesses and Lagrange multipliers for the gearbox.

Boundary conditions are applied to solve for the Eigenvectors. To plot these, the reduced coordinates and boundary conditions are added back into the Eigenvectors. Several modeshapes can be plotted. The y-axis is not relevant, since the scaling is done random.

The indices of the reduced mass and stiffness matrices are stored and sorted according to section 4.2.

Using a for loop with different section lengths the model consistency can be obtained.

#### **B.4.2 Data preprocessing**

Acceleration measurements are done (externally) using Labview and saved as .dat file. These can be imported by Matlab. Matlab routine *detrend* is used to remove the offset of each accelerometer. Matlab routine *fft* is used to get the Fourier transform of each accelerometer. A bandpass filter is used to remove higher harmonics from the signal. With the known rotational frequency the accelerations are converted to displacements.

#### **B.4.3 Loads to accelerations**

Using the assumed harmonic rotor force and known displacements and loads the motion of the test bench is predicted by solving the system of equations.

#### **B.4.4 Acceleration to loads**

Using the determined displacements from the accelerometers and known displacements or loads the motion of the test bench is predicted by solving the system of equations.